

Structural transformations in nonstoichiometric $\text{YBa}_2\text{Cu}_3\text{O}_{6+\delta}$

S. Semenovskaya and A. G. Khachatryan

Department of Materials Science and Engineering, Rutgers University, P.O. Box 909, Piscataway, New Jersey 08855-0909

(Received 20 November 1991)

Structural-transformation kinetics in $\text{YBa}_2\text{Cu}_3\text{O}_{6+\delta}$ caused by oxygen ordering is considered. The effect of long-range interaction between oxygen atoms, Coulomb repulsion, and strain-induced interaction on oxygen ordering is investigated in terms of crystal-lattice-site diffusion theory. Computer simulations of the diffusion of interacting O atoms give a complicated sequence of atomic-scale and mesoscale structural transformations. It is shown that the transformation path strongly influences the crystallographic structure of the ordered phases. An interrelation between the mesoscale and the atomic structures, which proves to be coupled by the long-range interaction, is found. The following structures are obtained: the primary tweed which transforms into a (110) polytwin structure, the secondary tweed, and the "glassy" state, as well as $2a_0 \times 2a_0$ and $2\sqrt{2}a_0 \times 2\sqrt{2}a_0$ superstructures. Two structural states, the secondary tweed and the "glassy" state, are shown to be mesoscopic phases—metastable (or stable) phases whose phase identity is mostly determined by their mesoscale rather than atomic-scale structure. The structures and morphologies generated in this computer simulation were reported in many experimental studies.

I. INTRODUCTION

As is known, the high-temperature superconducting $\text{YBa}_2\text{Cu}_3\text{O}_{6+\delta}$ can be regarded as an interstitial solid solution of oxygen based on the tetragonal insulating $\text{YBa}_2\text{Cu}_3\text{O}_6$ phase. A unit cell of $\text{YBa}_2\text{Cu}_3\text{O}_6$ is formed by three piled-up perovskite unit cells $a_0 \times a_0 \times 3a_0$ (where a_0 is the perovskite lattice parameter). The interstitial sites form two interpenetrating, crystallographically equivalent sublattices with the same crystal-lattice parameters [Fig. 1(a)]. A random distribution of O atoms over these two sublattices gives the disordered tetragonal $\text{YBa}_2\text{Cu}_3\text{O}_{6+\delta}$ phase (T phase). The ordering resulting in a preferential oxygen occupation of one of the sublattices (for example, the second sublattice) produces the orthorhombic polymorph O -I [Fig. 1(b)]. In the completely ordered state, its stoichiometric formula is $\text{YBa}_2\text{Cu}_3\text{O}_7$. This compound is the high-temperature superconductor. The $T \rightarrow O$ -I ordering is not the only one observed in this system. Another observed stable phase having the stoichiometry $\text{YBa}_2\text{Cu}_3\text{O}_{6.5}$ is O -II.¹⁻⁶ It is a double-period $2a_0 \times a_0 \times 3a_0$ phase, which will also be designated the $2a_0 \times a_0$ phase. Its structure is illustrated in Fig. 1(c).

It is interesting that in the nonstoichiometric oxides $\text{YBa}_2\text{Cu}_3\text{O}_{6+\delta}$, besides the O -I and O -II phases, a variety of other ordered states have been found: $2a_0 \times 2a_0$,⁵ small "patches" with $3a_0 \times a_0$, $4a_0 \times a_0$, and $5a_0 \times a_0$ ordered structures⁵ (diffraction maxima corresponding to these structures have also been reported^{1,3,6}), and the $2\sqrt{2}a_0 \times 2\sqrt{2}a_0$ ordered structure.^{5-7,9} It is believed that all observed ordered structures differ only in the distribution of oxygen atoms over the interstitial sites. There are indications that at room temperature nonstoichiometric $\text{YBa}_2\text{Cu}_3\text{O}_{6+\delta}$ usually exists in a form of a stable or metastable coherent mixture of microdomains of the O -II phase. This state has been interpreted as the

short-range-order (SRO) state.^{3-6,10} Sometimes, depending on the stoichiometry, diffuse maxima from these states vary from the $(\frac{1}{2}00)$ point corresponding to the O -II phase to $\sim(\frac{1}{3}00)$ point in the reciprocal space.^{3,6} Although a decomposition into a mixture of ordered phases or a mixture of ordered and disordered phases is usually expected in systems with several stable ordered intermediate phases, it should be emphasized, however, that to date there is no convincing experimental data which would confirm such a decomposition in the $\text{YBa}_2\text{Cu}_3\text{O}_{6+\delta}$ system.

To understand the origin of the variety of ordered states in the $\text{YBa}_2\text{Cu}_3\text{O}_{6+\delta}$ system and its unusual behavior, different from that in systems with ordered intermetallics, we have to formulate a model that would reflect the basic specific features of $\text{YBa}_2\text{Cu}_3\text{O}_{6+\delta}$, distinguishing it from the metal systems.

The main difference is that $\text{YBa}_2\text{Cu}_3\text{O}_{6+\delta}$ is a ceramic compound with a long-range repulsive Coulombic interaction between ions of the same kind. The theoretical calculations of ceramic oxides structure¹¹ and, specifically, the calculations of atomic structure and ionic and electronic defects in $\text{YBa}_2\text{Cu}_3\text{O}_7$,¹²⁻¹⁶ have proved this convincingly. For example, it has been shown that the Coulombic interaction accounts for approximately 90% of the total crystal lattice energy.¹⁴

The introduction of an oxygen atom into the crystal lattice of the tetragonal $\text{YBa}_2\text{Cu}_3\text{O}_6$ structure results in a crystal-lattice distortion. Overlapping strain fields generated by different O atoms yield the strain-induced O-O interaction. To describe the structural transformations in the $\text{YBa}_2\text{Cu}_3\text{O}_{6+\delta}$ system, the strain-induced interaction between O atoms should also be included in the model. In the harmonic approximation, the O-O strain-induced interaction is reduced to the pairwise interaction energies between the interstitial atoms.^{17,18} An important factor

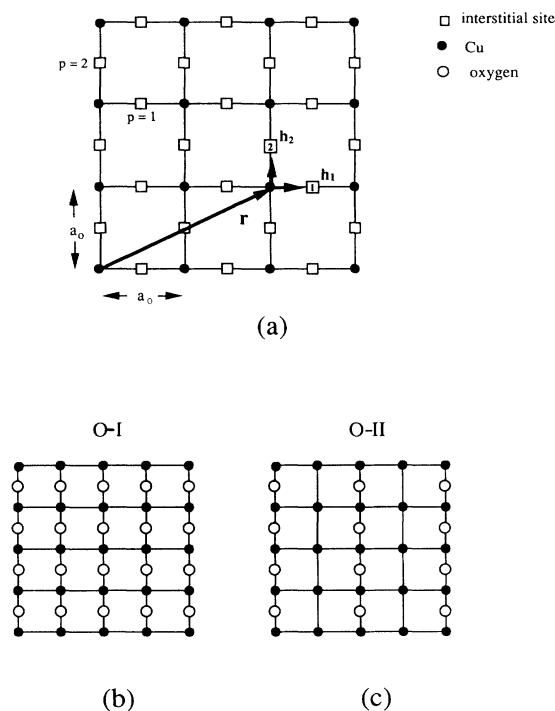


FIG. 1. The (001) Cu-O basal plane in $\text{YBa}_2\text{Cu}_3\text{O}_{6+\delta}$. (a) The basal plane of the tetragonal $\text{YBa}_2\text{Cu}_3\text{O}_6$ host lattice, (b) the $\text{YBa}_2\text{Cu}_3\text{O}_7$ orthorhombic phase, and (c) the $\text{YBa}_2\text{Cu}_3\text{O}_{6.5}$ double-period orthorhombic *O-II* phase are presented. Cu atoms are shown by solid circles. Interstitial sites belonging to two sublattices ($p = 1, 2$) are indicated in (a) by squares; vectors \mathbf{h}_1 and \mathbf{h}_2 show the position of the interstitial sublattice, $p = 1$ and 2; vector \mathbf{r} labels the Cu atom (in the host sublattice).

predetermining the special role played by the strain-induced interaction is an infinite interaction radius of the strain-induced pairwise potentials, which are highly directionally anisotropic; specifically, they have a dipole-dipolelike asymptotic behavior with the $1/r^3$ dependence on a separation distance r . This circumstance results in a useful analogy between this (and similar) systems and ferromagnetic and ferroelectrics whose magnetostatic and electrostatic energies are also determined by the infinite-radius dipole-dipole interaction. The dipole-dipole interaction, even being very small, results in an instability of a homogeneous single-domain state of a product phase with respect to a formation of domain patterns accommodating the magnetostatic and electrostatic energies. A situation with the strain-induced interaction is similar. An accommodation of the strain energy results in an instability of a homogeneous product phase with respect to a formation of domain patterns (polytwin patterns) consisting of orientation variants of the product phase.^{17–19} The strain-induced interaction, as any dipole-dipolelike interaction, modifies the classical Gibbs thermodynamics since the total volume-dependent energy becomes a function of microstructure, shape, orientation, and spatial distribution of orientation variants of the product phase. The twin and twinned self-organized patterns observed in $\text{YBa}_2\text{Cu}_3\text{O}_{6+\delta}$,^{1,8,20–27} as in numerous other systems, are

a direct consequence of this effect. Therefore, this is the long-range repulsion between the ordering oxygen atoms as well as their long-range strain-induced interaction that, actually, predetermines the peculiarities of structural transformations during the oxygen ordering in this material.

The existing short-range-interaction (SRI) model of oxygen ordering in $\text{YBa}_2\text{Cu}_3\text{O}_{6+\delta}$ (Refs. 28–36) cannot describe ordered states (other than *O-I* and *O-II*) observed in this system,^{1,3,5–9} and, obviously, cannot describe the twinned and polytwin patterns whose appearance is related to the long-range (strain-induced) interaction. However, the SRI model is a reasonable first (and the simplest possible) approximation that is able to describe the *T*, *O-I*, and *O-II* phases. Its main advantage is that the short interaction radius enables one to employ the CVM and Monte Carlo methods for the thermodynamic characterization of these phases.^{28–34,36} For the longer-range interaction these methods face insurmountable difficulties. [It is sometimes claimed that the first-principles calculation by Sterne and Wille³⁷ proves the validity of the three-neighbor SRI model. However, to prove this claim one has to do two things: (i) fit the interaction potentials so that the total configurational energies of several ordered phases calculated within the SRI model would be equal to the energies of the same phases obtained by the first-principles calculations, and (ii) find that the interaction potentials beyond a three-neighbor distance are zero or negligible. Item (ii) has not been done.]

A less obvious but very interesting fact is that any SRI model is “unstable” with respect to even a weak Coulombic addition to the O-O interaction potentials. Such an addition, which is expected for ceramic oxides, would radically change the phase diagram following from the SRI model. It would completely eliminate the two-phase fields among the *T*, *O-I*, and *O-II* phases since any spatial separation of oxygen ions required by the formation of a two-phase mixture violates local charge neutrality and, thus, increases the electrostatic energy. The larger the regions occupied by the oxygen-rich phase, the greater the increase. Instead of a two-phase mixture, the ordered states accommodating each current stoichiometry should be formed. A detailed investigation of this effect in two dimensions has been carried out by Aligia *et al.*^{15,16} for $\text{YBa}_2\text{Cu}_3\text{O}_{6+\delta}$.

A purpose of the present study is an investigation of the effect of the long-range interactions, typical for ceramic oxides, on structural transformations in $\text{YBa}_2\text{Cu}_3\text{O}_{6+\delta}$. This compound, besides its importance as a high-temperature superconductor, is an excellent particular case illustrating the generic properties of oxide ordering systems with predominantly repulsive interatomic interaction and with the phase transformations reducing the crystal-lattice point symmetry. We suggest a model which includes both the long-range Coulomb-like repulsive interaction and the strain-induced interaction between ordering oxygen atoms. This model will be employed to investigate the kinetics of structural transformations in $\text{YBa}_2\text{Cu}_3\text{O}_{6+\delta}$ using a computer-simulation technique based on the crystal-lattice-site diffusion theory.³⁸ The kinetic approach proposed in this study,

actually, does not use any *a priori* assumptions concerning possible atomic and mesoscale structures that may appear along the transformation path. No structural information other than the host-lattice geometry and the interatomic potentials has been introduced. The obtained structures automatically appear in the course of the computer simulation of the crystal-lattice-site diffusion.

The authors have used this method recently to study ordering in $\text{YBa}_2\text{Cu}_3\text{O}_7$.³⁹ It has been shown that the ordering in $\text{YBa}_2\text{Cu}_3\text{O}_7$ is accompanied by the tweed pattern formation that later transforms into a polytwin structure in the course of the strain-energy accommodation. Below, we extend this method to study the ordering transformations in nonstoichiometric $\text{YBa}_2\text{Cu}_3\text{O}_{6+\delta}$ over a wide range of stoichiometries and temperatures. Recently, a similar technique has been employed to study the structural-transformation kinetics during the precipitation of an ordered intermetallic phase from a disordered matrix.^{40,42}

II. COMPUTER-SIMULATION MODEL

A. Thermodynamic model

To describe the oxygen ordering in $\text{YBa}_2\text{Cu}_3\text{O}_{6+\delta}$, the Ising model is used. All structural states in this system can be obtained by considering the oxygen-atom redistribution over two sublattices of interstitial sites located in basal Cu-O (001) planes of the $a_0 \times a_0 \times 3a_0$ structure of the $\text{YBa}_2\text{Cu}_3\text{O}_6$ phase separated by three perovskite unit cells. These sublattices are displaced by the distances $\mathbf{h}_1 = a_0(\frac{1}{2}, 0, 0)$ and $\mathbf{h}_2 = a_0(0, \frac{1}{2}, 0)$ from the Cu-atom sublattice generated by Cu atoms occupying the apexes of $a_0 \times a_0 \times 3a_0$ unit cells [Fig. 1(a)]. Therefore, each interstitial position may be denoted (p, \mathbf{r}) , where \mathbf{r} is the translation vector labeling the Cu atom nearest the relevant interstitial site, and the index p labels the sublattice ($p = 1, 2$) of the interstitial site. The vector indicating the interstitial position is $\mathbf{h}_p + \mathbf{r}$. The positions of interstitial sites in (001) basal Cu-O planes are shown in Fig. 1(a). The distribution of O atoms over interstitial sites is characterized by the function $n(p, \mathbf{r})$, the occupation probability of finding an O atom in the interstitial site (p, \mathbf{r}) . In the disordered tetragonal T phase, oxygen atoms are randomly distributed over interstitial sites of both interstitial sublattices. Therefore, in the disordered T phase, $n(p, \mathbf{r}) = c = \text{const}$, where c is the fraction of interstitial sites of both sublattices occupied by O atoms. The concentration of O atoms, c , is directly related to the stoichiometry parameter δ by the equation

$$\delta = 2c .$$

Ordering leads to a particular dependence of $n(p, \mathbf{r})$ on the coordinates. In the completely ordered state, the function $n(p, \mathbf{r})$ assumes only two values, 1 and 0. If, for example, $n(p, \mathbf{r})$ depends only on p but does not depend on \mathbf{r} , i.e., if $n(p, \mathbf{r}) = n_p$, then this function describes an ordering resulting in the preferential occupation of one of the sublattices caused by the transfer of O atoms from another. In the completely ordered state, in which one of the sublattices is fully occupied while the other is fully

vacant, the ordering shown in Fig. 1(b) generates the orthorhombic high-temperature superconducting compound $\text{YBa}_2\text{Cu}_3\text{O}_7$.

1. Free energy

As has been mentioned above, the O-O interaction in $\text{YBa}_2\text{Cu}_3\text{O}_{6+\delta}$, as in most ceramic oxides, is long ranged.¹¹⁻¹⁶ In this case the mean-field approximation for the free energy is reasonably good, especially in the presence of the strain-induced interaction.⁴³ It becomes especially accurate, irrespective of the interaction radius, at comparatively low temperatures, where the long-range-order (LRO) parameter is large.⁴⁴ Using the mean-field approximation, we can present the free-energy functional in the following form:⁴⁵

$$F = \frac{1}{2} \sum_{p, \mathbf{r}} \sum_{q, \mathbf{r}'} W_{pq}(\mathbf{r} - \mathbf{r}') n(p, \mathbf{r}) n(q, \mathbf{r}') + k_B T \sum_{p, \mathbf{r}} \{ n(p, \mathbf{r}) \ln n(p, \mathbf{r}) + [1 - n(p, \mathbf{r})] \ln [1 - n(p, \mathbf{r})] \} , \quad (1)$$

where $W_{pq}(\mathbf{r} - \mathbf{r}')$ is the interaction energy of an O-atom pair with the O atoms located at the sites (p, \mathbf{r}) and (q, \mathbf{r}') , k_B is the Boltzmann constant, and T is the absolute temperature. The concentration-wave method developed in Ref. 45 allows one to deduce the ordering temperature T_1 and the superlattice vector from the pairwise interaction potentials $W_{pq}(\mathbf{r} - \mathbf{r}')$.

2. Ordering temperatures

At high temperature this free energy (1) is minimized at the probabilities $n(p, \mathbf{r}) = c$ that describe the disordered state. At low temperatures the disordered state loses its stability with respect to the concentration wave generating the ordered structure. The order-disorder temperature corresponding to this instability is determined by the bifurcation point of the equilibrium equation following from minimizing (1). It is equal to

$$T_1(c) = - \frac{c(1-c)}{k_B} \min[\lambda_\sigma(\mathbf{k})] , \quad (2)$$

where $\min[\lambda_\sigma(\mathbf{k})]$ means the absolute minimum of the function $\lambda_\sigma(\mathbf{k})$; \mathbf{k} is the wave vector defined in the first Brillouin zone of the parent tetragonal phase.⁴⁵ The function $\lambda_\sigma(\mathbf{k})$ is the eigenvalue of the Fourier transform of the interaction potential matrix,

$$V_{pq}(\mathbf{k}) = \sum_{\mathbf{r}} W_{pq}(\mathbf{r}) \exp(-i\mathbf{k} \cdot \mathbf{r}) , \quad (3)$$

i.e., $\lambda_\sigma(\mathbf{k})$ meets the secular equation

$$\sum_{q=1}^{q=2} V_{pq}(\mathbf{k}) v_\sigma(q, \mathbf{k}) = \lambda_\sigma(\mathbf{k}) v_\sigma(p, \mathbf{k}) , \quad (4a)$$

where the index $\sigma = 1, 2$ (or \pm) enumerates two branches of spectrum of the matrix $W_{pq}(\mathbf{r} - \mathbf{r}')$; $v_\sigma(p, \mathbf{k})$ is the eigenvector. This equation has a nontrivial solution if the determinant of the system (4a) vanishes:

$$\det \begin{bmatrix} V_{11}(\mathbf{k}) - \lambda & V_{12}(\mathbf{k}) \\ V_{12}^*(\mathbf{k}) & V_{22}(\mathbf{k}) - \lambda \end{bmatrix} = 0. \quad (4b)$$

The solution of the quadratic equation (4b) with respect to λ determines two branches of $\lambda_\sigma(\mathbf{k})$:

$$\lambda_{\pm}(\mathbf{k}) = \frac{1}{2}(V_{11}(\mathbf{k}) + V_{22}(\mathbf{k})) \pm \{ [V_{11}(\mathbf{k}) - V_{22}(\mathbf{k})]^2 + 4|V_{12}(\mathbf{k})|^2 \}^{1/2}. \quad (5)$$

By definition (5), the minimum of $\lambda_\sigma(\mathbf{k})$ is described by the minimum of the function $\lambda_{-}(\mathbf{k})$ with respect to \mathbf{k} , i.e.,

$$\min[\lambda_\sigma(\mathbf{k})] = \min[\lambda_{-}(\mathbf{k})] = \lambda_{-}(\mathbf{k}_0), \quad (6)$$

where \mathbf{k}_0 minimizes the $\lambda_{-}(\mathbf{k})$. The vector \mathbf{k}_0 found this way is the superlattice vector of the ordered phase. Therefore, Eqs. (2), (5), and (6) determine the structure of the ordered phase and the ordering temperature $T_1(c)$ through the matrix $V_{pq}(\mathbf{k})$.

If the minimum of $\lambda_{-}(\mathbf{k})$ falls at $\mathbf{k} = \mathbf{k}_0 = \mathbf{0}$, which is the case for the observed $T \rightarrow O$ -I transition, then the ordering results in the transition of O atoms from one sublattice to another sublattice and it is described by the occupation probability function $n(p, \mathbf{r}) = n_p$, which depends solely on the sublattice number p , but does not depend on the crystal-lattice-site coordinate \mathbf{r} . This probability distribution describes the orthorhombic phase O -I, which is the stoichiometric $\text{YBa}_2\text{Cu}_3\text{O}_7$ phase at $c = \frac{1}{2}$ [Fig. 1(b)].

If the composition deviates from the stoichiometry $c = \frac{1}{2}$ (i.e., $\delta = 2c < 1$) and if the decomposition into a mixture of T and O -I stoichiometric phases is hindered, then the secondary ordering occurs. The disordered phase for the secondary ordering is the orthorhombic O -I phase described by $n(p, \mathbf{r}) = n_p$. According to Ref. 46, the secondary ordering temperature $T_2(c)$ can be found from equation

$$T_2(c) = - \frac{\min[\Lambda_\sigma(\mathbf{k})]}{k_B}, \quad (7a)$$

where $\Lambda_\sigma(\mathbf{k})$ is the eigenvalue spectrum of the 2×2 Hermitian matrix:

$$\tilde{V}_{pq}(\mathbf{k}) = \sqrt{n_p(1-n_p)} V_{pq}(\mathbf{k}) \sqrt{n_q(1-n_q)}. \quad (7b)$$

The fact that the stable secondary ordered phase O -II in this system [Fig. 1(c)] is characterized by the $(\frac{1}{2}, 0, 0)$ superlattice vector, actually, means that the interaction potential is such that the minimum of the eigenvalue $\Lambda_\sigma(\mathbf{k})$ falls at $\mathbf{k}_1 = (2\pi/a_0)(\frac{1}{2}, 0, 0)$.

B. Interaction model

The $\text{YBa}_2\text{Cu}_3\text{O}_{6+\delta}$ are, actually, interstitial solid solutions of oxygen atoms based on the tetragonal $\text{YBa}_2\text{Cu}_3\text{O}_6$ phase. As is known, the oxygen ordering in $\text{YBa}_2\text{Cu}_3\text{O}_{6+\delta}$ occurs in the basal (001) planes separated by three layers of the perovskite lattice. The interaction between the oxygen atoms located in different basal planes in this system is much weaker than that within the plane. The diffusion of O atoms is almost planar since

the oxygen diffusion within the basal plane occurs substantially faster than the diffusional exchange between the different basal planes.⁴⁷ For such a system it is reasonable to start from the two-dimensional (2D) model, which would be the first approximation of the structural transformation kinetics problem. An extension to the 3D model is straightforward and does not pose any serious additional problems since the thermodynamic equations formulated above and the kinetic equations considered below are valid in the 3D case as well. The only problem is that the 3D model requires more information on O-O interaction potentials and would take a longer time to compute. We consider below the 2D square crystal lattice composed of Cu atoms shown in Fig. 1(a). It is the basal (001) plane of $\text{YBa}_2\text{Cu}_3\text{O}_6$. Interstices of this lattice are located between the nearest Cu atoms. They are partially occupied by the interacting O atoms which can migrate.

The Fourier transform of the O-O interaction potential, $V_{pq}(\mathbf{k})$, has its singularity at $\mathbf{k} = \mathbf{0}$. The singularity is introduced by the strain-induced interaction. The point $\mathbf{k} = \mathbf{0}$ is a bifurcation point. Its origin is associated with a degeneracy of the acoustic-phonon spectrum at $\mathbf{k} = \mathbf{0}$, which is related to an invariance of the energy with respect to the rigid-body translations. It is this singularity that results in an infinite range radius of the pairwise interaction. Its long-range asymptote has a dipole-dipolelike behavior. If we single out the singular part, $B_{pq}(\mathbf{k})$, from $V_{pq}(\mathbf{k})$ so that

$$V_{pq}(\mathbf{k}) = B_{pq}(\mathbf{k}) + V_{pq}^f(\mathbf{k}), \quad (8)$$

then the remaining part, $V_{pq}^f(\mathbf{k})$, is analytical at all real values of \mathbf{k} . Because of that, its back-Fourier-transform, $W_{pq}^f(\mathbf{r})$, asymptotically decreases with the separation distance r as $\exp(-r/r_0)$, where r_0 is the interaction radius. Therefore, the interaction energies $W_{pq}^f(\mathbf{r})$ describe the finite-radius interaction. We assume that the $W_{pq}^f(\mathbf{r})$ are reasonably well approximated by the anisotropic screened-Coulomb repulsive potential proposed by Aligia *et al.*¹⁶

1. Strain-induced interaction potentials

Since $B_{pq}(\mathbf{k})$ has the singularity at $\mathbf{k} = \mathbf{0}$, its long-distance asymptote is described by the continuum elasticity. The continuum elasticity theory gives the following approximation for $B_{pq}(\mathbf{k})$ near $\mathbf{k} = \mathbf{0}$:^{46,18}

$$B_{pq}(\mathbf{k}) \approx -vm_i\sigma_{ij}(p)\Omega_{jk}(\mathbf{m})\sigma_{kl}(q)m_l \exp[i\mathbf{k} \cdot (\mathbf{h}_p - \mathbf{h}_q)], \quad (9)$$

where $\sigma_{ij}(p) = c_{ijkl}\varepsilon_{kl}^0(p)$, $\varepsilon_{kl}^0(p)$ is the tensor of the concentrational crystal-lattice expansion coefficients associated with O atoms in the p th interstitial sublattice, c_{ijkl} is the elastic strain modulus tensor, v is the unit-cell volume, $\Omega_{jk}(\mathbf{m})$ is the Green tensor reciprocal to the tensor $\Omega_{jk}^{-1}(\mathbf{m}) = c_{jilk}m_jm_l$, and $\mathbf{m} = \mathbf{k}/k$. To calculate $B_{pq}(\mathbf{k})$, we have to specify the parameters entering (9). The 2D components of the concentration expansion tensor $\varepsilon_{kl}^0(p)$ along the x and y ([100] and [010]) axes are

$$\varepsilon_{kl}^0(1) = \begin{bmatrix} \varepsilon_{22} & 0 \\ 0 & \varepsilon_{11} \end{bmatrix}, \quad \varepsilon_{kl}^0(2) = \begin{bmatrix} \varepsilon_{11} & 0 \\ 0 & \varepsilon_{22} \end{bmatrix}, \quad (10)$$

where $\varepsilon_{kl}^0(1)$ and $\varepsilon_{kl}^0(2)$ characterize the distortions caused by introducing the oxygen atoms into the first ($p=1$) and the second ($p=2$) sublattices, respectively; ε_{22} and ε_{11} are the corresponding elongation and contraction deformations. Assuming that $\varepsilon_{22} = -\varepsilon_{11} = \varepsilon_0$, we may rewrite Eq. (10) in the form

$$\varepsilon_{kl}^0(1) = \varepsilon_0 \begin{bmatrix} 1 & 0 \\ 0 & -1 \end{bmatrix}, \quad \varepsilon_{kl}^0(2) = -\varepsilon_0 \begin{bmatrix} 1 & 0 \\ 0 & -1 \end{bmatrix}. \quad (11)$$

With the definition of nonzero components of the elastic moduli tensor c_{ijkl} for the tetragonal host lattice, $c_{xxxx} = c_{yyyy} = c_{11}$, $c_{xxyy} = c_{12}$, and $c_{xyxy} = c_{66}$, we can express the nonvanishing components of the Green tensor $\Omega_{jk}(\mathbf{m})$ in the x - y plane as

$$\begin{aligned} \Omega_{xx}(\mathbf{m}) &= [c_{66} + (c_{11} - c_{66})m_y^2]/D(\mathbf{m}), \\ \Omega_{yy}(\mathbf{m}) &= [c_{66} + (c_{11} - c_{66})m_x^2]/D(\mathbf{m}), \\ \Omega_{xy}(\mathbf{m}) &= -[(c_{12} + c_{66})m_x m_y]/D(\mathbf{m}), \end{aligned} \quad (12a)$$

where $D(\mathbf{m}) = c_{66}[c_{11} + \phi(c_{11} + c_{12})m_x^2 m_y^2]$,

$$\phi = (c_{11} - c_{12} - 2c_{66})/c_{66}, \quad (12b)$$

and $\mathbf{m} = \mathbf{k}/k = (m_x, m_y)$. Using the definition $\sigma_{ij}(p) = c_{ijkl}\varepsilon_{kl}^0(p)$ and Eqs. (12a) in (9) gives

$$\begin{aligned} B_{pq}(\mathbf{k}) &= -v(c_{11} - c_{12})^2 \frac{\varepsilon_0^2}{c_{66}} \Phi(\mathbf{m}) \begin{bmatrix} 1 & -1 \\ -1 & 1 \end{bmatrix} \\ &\quad \times \exp[i\mathbf{k} \cdot (\mathbf{h}_p - \mathbf{h}_q)], \end{aligned} \quad (13)$$

where

$$\Phi(\mathbf{m}) = \frac{c_{66} + 2(c_{11} + c_{12})m_x^2 m_y^2}{c_{11} + \phi(c_{11} + c_{12})m_x^2 m_y^2}. \quad (14)$$

Using the lattice parameters for $\text{YBa}_2\text{Cu}_3\text{O}_7$ obtained in Ref. 48, $a = 3.822 \text{ \AA}$, $b = 3.891 \text{ \AA}$, $c = 11.677 \text{ \AA}$, and $a_t \approx (a + b)/2 = 3.856 \text{ \AA}$, we have

$$\begin{aligned} \varepsilon_{22} &= (b - a_t)/a_t \approx \varepsilon_0 = 0.009, \\ \varepsilon_{11} &= (a - a_t)/a_t \approx -\varepsilon_0 = -0.009, \\ v &= abc = 173 \text{ \AA}^3. \end{aligned} \quad (15)$$

The elastic constants calculated in Ref. 13 give the estimate

$$\begin{aligned} c_{11} &\approx 3.9 \times 10^{12} \text{ dyn/cm}^2, \\ c_{12} &\approx 1.36 \times 10^{12}, \\ c_{66} &\approx 0.91 \times 10^{12}. \end{aligned} \quad (16)$$

Using the numerical data (15) and (16) in (13) and (14) yields

$$v \frac{(c_{11} - c_{12})^2 \varepsilon_0^2}{c_{66}} \approx 993 \times 10^{-16} \text{ erg} = (719 \text{ K})k_B, \quad (17)$$

$$\Phi(\mathbf{m}) = 0.2333 \frac{1 + 11.558m_x^2 m_y^2}{1 + 1.066m_x^2 m_y^2}. \quad (18)$$

The final expression for $B_{pq}(\mathbf{k})$ (in K) for any wave vector (within the first Brillouin zone of the disordered tetragonal phase) with the above numerical data for $\text{YBa}_2\text{Cu}_3\text{O}_7$ has the form

$$\begin{aligned} B_{pq}(\mathbf{k}) &= -(168 \text{ K})k_B \frac{1 + 11.558m_x^2 m_y^2}{1 + 1.066m_x^2 m_y^2} \begin{bmatrix} 1 & -1 \\ -1 & 1 \end{bmatrix} \\ &\quad \times \exp[i\mathbf{k} \cdot (\mathbf{h}_p - \mathbf{h}_q)]. \end{aligned} \quad (19)$$

As has been emphasized above, Eq. (9) gives the long-wave approximation of the strain-induced O-O potentials valid at small \mathbf{k} , $k \ll 2\pi/a_0$. This approximation is, actually, very good for the $T \rightarrow O$ -I ordering in $\text{YBa}_2\text{Cu}_3\text{O}_{6+\delta}$ oxides since the ordering is induced by an antisymmetric irreducible representation of the space group related to the vector $\mathbf{k} = 0$. Therefore, the ordering is described by the concentration wave packet whose wave vectors \mathbf{k} are located in a vicinity of $\mathbf{k} = 0$ where the approximation (9) holds.

At $\mathbf{k} \rightarrow 0$, the function $B_{pq}(\mathbf{k})$ described by Eq. (19) has a very strong dependence on the wave-vector direction \mathbf{m} , but does not depend on the absolute value of \mathbf{k} . This is a reason why its back-Fourier-transform, describing the pairwise strain-induced interactions between O atoms, has the dipole-dipolelike asymptotic behavior decaying with the separation distance as r^{-3} .

2. Finite-radius potentials $W_{pq}^f(r - r')$

The function $V_{pq}^f(\mathbf{k})$ is the Fourier transform of the finite-radius interaction between oxygen atoms, $W_{pq}^f(\mathbf{r} - \mathbf{r}')$. The potential $W_{pq}^f(\mathbf{r} - \mathbf{r}')$ characterizes repulsive interaction energies of oxygen-ion pairs. We describe it as a screened-Coulomb potential supplemented by the nearest-neighbor correction and by the next-nearest-neighbor anisotropic correction [as it follows from Fig. 1(a), the next-nearest interstitial sites always belong to the same sublattice]:

$$W_{pq}^f(\mathbf{r} - \mathbf{r}') = \begin{cases} \frac{(z^*)^2}{a_0/\sqrt{2}} \exp\left[-\frac{a_0/\sqrt{2}}{r_D}\right] + \delta W_1 & \text{for the nearest sites at } |\mathbf{r} + \mathbf{h}_p - \mathbf{r}' - \mathbf{h}_q| = a_0/\sqrt{2}, \\ (1 \pm f) \frac{(z^*)^2}{a_0} \exp\left[-\frac{a_0}{r_D}\right] & \text{for the next-nearest sites at } |\mathbf{r} - \mathbf{r}'| = a_0, \\ \frac{(z^*)^2}{|\mathbf{r} + \mathbf{h}_p - \mathbf{r}' - \mathbf{h}_q|} \exp\left[-\frac{|\mathbf{r} + \mathbf{h}_p - \mathbf{r}' - \mathbf{h}_q|}{r_D}\right] & \text{at } |\mathbf{r} + \mathbf{h}_p - \mathbf{r}' - \mathbf{h}_q| > a_0, \end{cases} \quad (20)$$

where z^* is the effective oxygen charge, r_D is the screening radius, f is the anisotropy constant which has a negative sign for O-O interaction across a Cu atom and positive sign otherwise. The anisotropic screened-Coulomb potential (20) has been used by Aligia *et al.*¹⁶ in a similar form. These authors, however, did not take into account the strain-induced interaction and correction δW_1 .

3. Values of parameters r_D , z^* , δW_1 , and f

The O-O finite-range interaction potentials (20) depend on the parameters r_D , z^* , δW_1 , and f . These parameters can be estimated by fitting the calculated and the observed order-disorder transition temperatures in $\text{YBa}_2\text{Cu}_3\text{O}_{6.5}$ for the primary $T \rightarrow O-I$ and the secondary $O-I \rightarrow O-II$ transitions. The assumption that $O-I$ and $O-II$ phases are stable should be also used.

The screening radius r_D can be estimated as follows. It cannot be too large, as the material has a comparatively high density of free charge carriers (holes). But it cannot be too small either, since then it cannot provide the stability of the double-period $O-II$ structure (it should be, at least, larger than its period, $2a_0$). We have chosen the value $r_D = 5a_0/\sqrt{2}$. We have also tested other values of r_D , $r_D = 3a_0/\sqrt{2}$, $r_D = 8a_0/\sqrt{2}$, and $r_D \rightarrow \infty$, and have found that the structural transformation sequence is not affected by these changes in the screening radius.

The most stable ordered structures are the structures generated by the concentration waves whose wave vectors correspond to the Lifshitz points in the first Brillouin zone of the disordered phase (the Lifshitz point is defined as a point within the first Brillouin zone whose point group has the symmetry elements intersecting in one point). At these points the minimum conditions, $\partial\lambda_\sigma(\mathbf{k})/\partial\mathbf{k} = 0$ and $\partial\Lambda_\sigma(\mathbf{k})/\partial\mathbf{k} = 0$, which according to (2), (6), and (7a) determine the structure of the most stable ordered phases, are automatically fulfilled. This occurs because of the crystal-lattice symmetry rather than any specific choice of the interaction potential. The first Brillouin zone of the disordered T phase and the primary ordered $O-I$ phase has only three stars of the Lifshitz points, (000) , $\{\frac{1}{2}00\}$, and $\{\frac{1}{2}\frac{1}{2}0\}$. It follows from the known structure of the $O-I$ phase that it is related to the (000) Lifshitz point. The structure is generated by the antisymmetric irreducible representation of the group of the vector $\mathbf{k}_0 = 0$. Since the $O-I$ structure is the most stable, $\mathbf{k} = 0$ provides the absolute minimum of $\lambda_-(\mathbf{k})$ [see Eq. (6)]. According to the observations,¹⁻⁶ another Lifshitz phase, $O-II$, related to the $\{\frac{1}{2}00\}$ Lifshitz point and generated by the secondary ordering, is also stable. This means that $\mathbf{k}_1 = (2\pi/a_0)(\frac{1}{2}, 0, 0)$ provides the absolute minimum of $\Lambda_\sigma(\mathbf{k})$. The third Lifshitz structure, generated by the vector $\mathbf{k}_2 = (2\pi/a_0)(\frac{1}{2}, \frac{1}{2}, 0)$, has been also reported in Ref. 5, but this $2a_0 \times 2a_0$ ordered structure is, however, a transient and, thus, is less stable than $\{\frac{1}{2}00\}$ Lifshitz structure. This means that $\Lambda_-(\mathbf{k}_1)$ is slightly less than $\Lambda_-(\mathbf{k}_2)$:

$$\Lambda_-(\mathbf{k}_1) < \Lambda_-(\mathbf{k}_2).$$

It should be remembered that the stability conditions de-

scribed above are applied to the total function $V_{pq}(\mathbf{k})$ including the term $B_{pq}(\mathbf{k})$ [see Eq. (8)].

The above-described stability conditions and the fitting to the temperatures $T_1(c)$ and $T_2(c)$ [Eqs. (2) and (7a); also see Fig. 2] of the primary $T \rightarrow O-I$ and the secondary $O-I \rightarrow O-II$ orderings impose severe limitations on the permitted values of parameters z^* , δW_1 , and f , entering (20) [the strain-induced interaction has been already determined by (19)]. We have tested different values of these parameters and have found that their specific values do not affect the structural transformation sequence as long as the above-formulated limitations are met. In this paper we will present the computer-simulation results for the specific choice of the parameters that gives the right values of $T_1(c)$ and $T_2(c)$ for $\text{YBa}_2\text{Cu}_3\text{O}_{6.5}$. The experimentally observed temperature $T_1(c)$ for the primary ordering is $T_1 \approx 970$ K.⁴⁹ According to Ref. 22, the isothermal reduction of $\text{YBa}_2\text{Cu}_3\text{O}_7$ inside the microscope under the constant beam current results in the appearance of $O-II$ phase reflections at 400°C. These reflections, however, have not been observed at 500°C. These observations give us the rough estimate for the maximum value of $T_2(c)$ at $\delta = 0.5$ to be around $T_2 \sim 720$ K.

The specific choice of the parameters meeting the above conditions are

$$z^* = 0.16e, \quad \delta W_1 = (476 \text{ K})k_B, \quad f = 0.5, \quad (21)$$

where e is the charge of the electron. These parameters

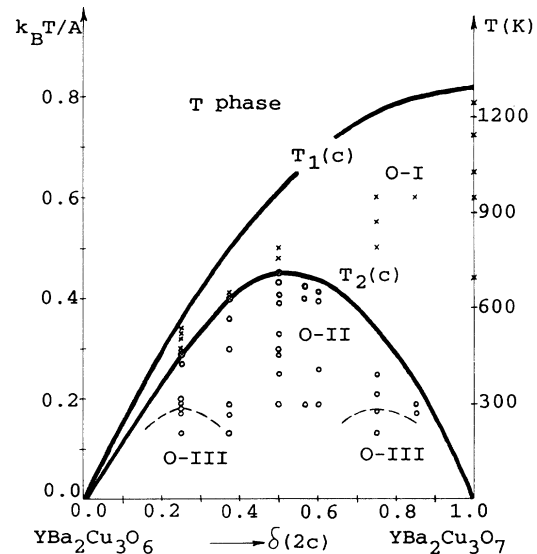


FIG. 2. The T - δ phase diagram of $\text{YBa}_2\text{Cu}_3\text{O}_{6+\delta}$ calculated with interaction parameters (19)–(21). The $T_1(c)$ and $T_2(c)$ lines describe the $T \rightarrow O-I$ and $O-I \rightarrow O-II$ order \leftrightarrow disorder temperatures. Dashed lines around the stoichiometries $\delta = \frac{1}{4}$ and $\frac{3}{4}$ give approximate temperatures for the $O-II \rightarrow O-III$ tertiary ordering, where $O-III$ is the $2\sqrt{2}a_0 \times 2\sqrt{2}a_0$ phase. Crosses and circles designate the stoichiometries and temperatures in the $O-I$ and $O-II$ fields, respectively, investigated in this computer simulation. The temperatures are given in the reduced scale, $T^* = k_B T/A$, and in the absolute scale (K) [$A = (z^*)^2 \sqrt{2}/a_0$ is determined by (21)].

also provide the relation

$$\Lambda_-(\mathbf{k}_2) = 0.7\Lambda_-(\mathbf{k}_1),$$

which demonstrates that $2a_0 \times 2a_0$ secondary phase is less stable than O -II phase since $\Lambda_-(\mathbf{k}_2) < 0$ and $\Lambda_-(\mathbf{k}_1) < 0$.

The ordering temperatures have been calculated from the following equations. The equation for the primary ordering temperature $T_1(c)$ follows from (2) and (5) at $\mathbf{k}=\mathbf{0}$:

$$T_1(c) = -\frac{c(1-c)}{k_B} [V_{11}(0) - |V_{12}(0)|]. \quad (22)$$

Equations (7) for $T_2(c)$ include values of occupation probabilities, n_1 and n_2 , in the first and second sublattices of the primary ordered O -I phase at $T=T_2(c)$. Calculations carried out with the choice of parameters (21) have demonstrated that, at the secondary ordering temperature $T_2 \sim 720$ K, we have $n_1 \approx 0$ and $n_2 \approx 2c = \delta$ at $\delta=0.5$. Under these conditions the only nonvanishing element of the 2×2 matrix (7b) is $\tilde{V}_{22}(\mathbf{k})$. Therefore,

$$\Lambda_-(\mathbf{k}) = \tilde{V}_{22}(\mathbf{k}) = 2c(1-2c)V_{22}(\mathbf{k}). \quad (23)$$

With (23), Eq. (7a) reads

$$T_2(c) = -\frac{2c(1-2c)V_{22}(\mathbf{k}_1)}{k_B}, \quad (24)$$

where $\mathbf{k}_1 = (2\pi/a_0)(\frac{1}{2}, 0, 0)$ since the minimum of $V_{22}(\mathbf{k})$ falls on this point. The Fourier transforms $V_{pq}(\mathbf{k})$ in Eqs. (22)–(24) include the strain-induced contribution (19).

C. Microscopic kinetic model

1. Crystal-lattice-site diffusion equation

For the computer simulation of the diffusion kinetics of ordering, we utilize the microscopic crystal-lattice-site diffusion equation:^{38,18,50}

$$\frac{dn(p, \mathbf{r}; t)}{dt} = \sum_{q=1}^{q=2} \sum_{\mathbf{r}'} L_{pq}(\mathbf{r}-\mathbf{r}') \frac{\delta F}{\delta n(q, \mathbf{r}'; t)}, \quad (25)$$

where $n(p, \mathbf{r}; t)$ is the occupation probability of finding an oxygen atom at site (p, \mathbf{r}) defined on the time-dependent ensemble, t is the time, F is the free-energy functional of

$$\left\{ \frac{\delta F}{\delta n(q, \mathbf{r}; t)} \right\}_{\mathbf{k}} = \sum_{s=1}^{s=2} \left[V_{qs}(\mathbf{k}) \bar{n}(s, \mathbf{k}; t) + \delta_{qs} k_B T \left\{ \ln \left[\frac{n(s, \mathbf{r}; t)}{1-n(s, \mathbf{r}; t)} \right] \right\}_{\mathbf{k}} \right]. \quad (31)$$

Substituting (8) for (31) and (31) for (27) yields the final form:

$$\frac{d\bar{n}(p, \mathbf{k}; t)}{dt} = \sum_{q=1}^{q=2} \sum_{s=1}^{s=2} \tilde{L}_{pq}(\mathbf{k}) \left[[V_{qs}^f(\mathbf{k}) + B_{qs}(\mathbf{k})] \bar{n}(s, \mathbf{k}; t) + \delta_{qs} k_B T \left\{ \ln \left[\frac{n(s, \mathbf{r}; t)}{1-n(s, \mathbf{r}; t)} \right] \right\}_{\mathbf{k}} \right]. \quad (32)$$

The reciprocal-space formulation (32) of the crystal-lattice-site diffusion describes a temporal evolution of $2N$ amplitudes $\bar{n}(p, \mathbf{k}; t)$ of the static concentration waves. It automatically includes the strain effect characterized by

the function $n(p, \mathbf{r}; t)$, and $L_{pq}(\mathbf{r}-\mathbf{r}')$ is the matrix of the kinetic coefficients (microscopic diffusional mobility) related to the expectation time of an elementary diffusional jump from site (q, \mathbf{r}') to site (p, \mathbf{r}) . The variational derivative, $\delta F/\delta n(q, \mathbf{r}; t)$, is the transformation driving force. The summation over \mathbf{r}' is carried out over all N unit cells of the crystal. Equations (25) are actually Önsager equations with respect to the $2N$ relaxing parameters $n(p, \mathbf{r}; t)$. They describe the crystal-lattice-site diffusion of interacting oxygen atoms. In the limit case of noninteracting atoms, the solution of Eq. (25) is reduced to the combinatorial solution of the random-walk problem. The long-wave limit of Eq. (25) is reduced to a Ginzburg-Landau equation, providing the microscopic interpretation of its phenomenological coefficients.

The equation for the thermodynamic driving force follows from (1):

$$\frac{\delta F}{\delta n(q, \mathbf{r}; t)} = \sum_{s, \mathbf{r}'} W_{qs}(\mathbf{r}-\mathbf{r}') n(s, \mathbf{r}; t) + k_B T \ln \frac{n(q, \mathbf{r}; t)}{1-n(q, \mathbf{r}; t)}. \quad (26)$$

It is very convenient to use the \mathbf{k} -space (Fourier) representation of the real-space kinetic equation (25) for the computer simulations. Multiplying (25) by $\exp(-i\mathbf{k}\cdot\mathbf{r})$ and summing it over all crystal-lattice sites gives

$$\frac{d\bar{n}(p, \mathbf{k}; t)}{dt} = \sum_{q=1}^{q=2} \tilde{L}_{pq}(\mathbf{k}) \left\{ \frac{\delta F}{\delta n(q, \mathbf{r}; t)} \right\}_{\mathbf{k}}, \quad (27)$$

where the symbol $\{(\dots)\}_{\mathbf{k}}$ determines the Fourier transform of the relevant function (\dots) :

$$\{(\dots)\}_{\mathbf{k}} = \sum_{\mathbf{r}} (\dots) \exp(-i\mathbf{k}\cdot\mathbf{r}),$$

$$\bar{n}(p, \mathbf{k}; t) = \{n(p, \mathbf{r}; t)\}_{\mathbf{k}} = \sum_{\mathbf{r}} n(p, \mathbf{r}; t) \exp(-i\mathbf{k}\cdot\mathbf{r}), \quad (28)$$

$$\tilde{L}_{pq}(\mathbf{k}) = \{L_{pq}(\mathbf{r})\}_{\mathbf{k}} = \sum_{\mathbf{r}} L_{pq}(\mathbf{r}) \exp(-i\mathbf{k}\cdot\mathbf{r}). \quad (29)$$

The conservation condition for the total number of O atoms requires that $\tilde{L}_{pq}(0)$ is reduced to the equation

$$\sum_{p, \mathbf{r}} L_{pq}(\mathbf{r}) = \sum_p \tilde{L}_{pq}(0) = 0. \quad (30)$$

The Fourier transform of the driving force (26) is equal to

the term $B_{qs}(\mathbf{k})$. Working in reciprocal space has several advantages: Eq. (32) is simpler than the finite-difference real-space equation (25); it allows one to incorporate an arbitrary long-range interaction without any computa-

tional complications and any adverse effect on the computation speed [the interaction radius does not affect the computational time when Eq. (32) is used]; and, finally, it allows us to use the fast-Fourier-transform algorithm, which dramatically accelerates all computations and, as a matter of fact, makes them possible.

2. Coefficients $\tilde{L}_{pq}(\mathbf{k})$

$\tilde{L}_{pq}(\mathbf{k})$ is the Fourier transform of the microscopic mobility coefficients $L_{pq}(\mathbf{r}-\mathbf{r}')$ related to the elementary diffusional jump of an O atom site from (q, \mathbf{r}') to site (p, \mathbf{r}) . In the relevant case of two interstitial sublattices $(p, q=1, 2)$, $\tilde{L}_{pq}(\mathbf{k})$ is the 2×2 matrix. Assuming that

the elementary diffusional jump may occur only between the nearest interstitial sites ($|\mathbf{r}+\mathbf{h}_1-\mathbf{r}'-\mathbf{h}_2|=a_0/\sqrt{2}$) [see Fig. 1(a)] that belong to the different sublattices, we have the only nonvanishing elements of the matrix $L_{pq}(\mathbf{r}-\mathbf{r}')$:

$$L_{pq}(\mathbf{r}-\mathbf{r}') = \begin{cases} L_1 & \text{if } |\mathbf{r}+\mathbf{h}_p-\mathbf{r}'-\mathbf{h}_q|=a_0/\sqrt{2}, \\ -4L_1 & \text{if } |\mathbf{r}+\mathbf{h}_p-\mathbf{r}'-\mathbf{h}_q|=0, \\ 0 & \text{otherwise,} \end{cases} \quad (33)$$

where the condition $L_{11}(0)=L_{22}(0)=-4L_1$ follows from Eq. (30) under the assumption that only nearest-neighbor diffusion jumps are permitted. The Fourier transform of the matrix (33) gives the 2×2 matrix:

$$\tilde{L}_{pq}(\mathbf{k}) = 4L_1 \begin{pmatrix} -1 & \cos(\mathbf{k} \cdot \mathbf{h}_1)\cos(\mathbf{k} \cdot \mathbf{h}_2)\exp[i\mathbf{k} \cdot (\mathbf{h}_1 - \mathbf{h}_2)] \\ \cos(\mathbf{k} \cdot \mathbf{h}_1)\cos(\mathbf{k} \cdot \mathbf{h}_2)\exp[-i\mathbf{k} \cdot (\mathbf{h}_1 - \mathbf{h}_2)] & -1 \end{pmatrix}. \quad (34)$$

D. Diffuse scattering generated by oxygen-induced elastic strain

As has been discussed above, introduction of O atoms into the tetragonal $\text{YBa}_2\text{Cu}_3\text{O}_6$ host lattice results in the host-lattice displacements and strain-induced O-O interaction associated with interference of displacement fields. The displacement field caused by such defects should generate the strong Huang-type diffuse scattering near the fundamental diffraction spots of the host lattice.⁵¹ The diffuse-scattering asymptotic behavior is proportional to $\sim 1/k^2$, where k is the distance from the fundamental spot. This scattering is actually associated with the interstitial-induced long-wave static acoustic displacement modes. Therefore, it can be described in terms of the continuum elasticity in a way similar to the

description of the strain-induced contribution to the interaction energy, $B_{pq}(\mathbf{k})$. Then, the Fourier components of the atomic displacements in an interstitial solid solution, $\tilde{u}(\mathbf{k})$, can be related to the Fourier transforms of the occupation probabilities of O atoms by the equation

$$\tilde{u}_j(\mathbf{k}) = -i \frac{1}{k} \Omega_{jk}(\mathbf{m}) \sum_{p=1}^2 \sigma_{kl}(p) m_l \tilde{n}(p, \mathbf{k}; t), \quad (35)$$

where $\Omega_{jk}(\mathbf{m})$, $\sigma_{kl}(p)$, and m_l are defined following Eq. (9).^{52,46,18} Using the components of the Green tensor $\Omega_{jk}(\mathbf{m})$ [Eq. (12)], we can present the displacement field, $\mathbf{u}(\mathbf{r})=(u_x(\mathbf{r}), u_y(\mathbf{r}))$, as the back-Fourier-transform of (35). The result reads

$$\begin{aligned} u(\mathbf{r})_x &= -i \frac{c_{11}-c_{12}}{c_{66}} \varepsilon_0 \frac{1}{N} \sum_{\mathbf{k}} \frac{1}{(k_x^2+k_y^2)^{1/2}} [\tilde{n}(1, \mathbf{k}; t) - \tilde{n}(2, \mathbf{k}; t)] \frac{c_{66} + (c_{11}+c_{12})m_y^2}{c_{11} + \phi(c_{11}+c_{12})m_x^2 m_y^2} m_x \exp(i\mathbf{k} \cdot \mathbf{r}), \\ u(\mathbf{r})_y &= i \frac{c_{11}-c_{12}}{c_{66}} \varepsilon_0 \frac{1}{N} \sum_{\mathbf{k}} \frac{1}{(k_x^2+k_y^2)^{1/2}} [\tilde{n}(1, \mathbf{k}; t) - \tilde{n}(2, \mathbf{k}; t)] \frac{c_{66} + (c_{11}+c_{12})m_x^2}{c_{11} + \phi(c_{11}+c_{12})m_x^2 m_y^2} m_y \exp(i\mathbf{k} \cdot \mathbf{r}), \end{aligned} \quad (36)$$

where $|\mathbf{k}|=(k_x^2+k_y^2)^{1/2}$; ε_0 and ϕ are determined in (15) and (12b). The displacement field is determined by Eq. (36) in terms of the Fourier transforms of the occupation probabilities $\tilde{n}(p, \mathbf{k}; t)$ at each time moment t , the temporal dependence of $\tilde{n}(p, \mathbf{k}; t)$ being described by the solution of the kinetic equation (32).

The diffuse-scattering intensity associated with the displacement field (36) is determined by the equation

$$I(2\pi\mathbf{H} + \mathbf{k}, t)_{\text{stat}} \sim \sum_{\mathbf{R}} |\exp[-i(2\pi\mathbf{H} + \mathbf{k})(\mathbf{r} + \mathbf{u}(\mathbf{r}))]|^2, \quad (37)$$

where \mathbf{H} is the fundamental reciprocal-lattice vector and $\mathbf{k}/2\pi$ is the distance of the measurement point from the fundamental reciprocal-lattice point \mathbf{H} .

E. Computational method

Structural transformations in the system under study are associated with the O atoms redistribution over interstitial sites of the basal (001) planes. In terms of the 2D Ising model formulated in the preceding sections, all structure transformations are described by temporal and spatial evolution of the occupation probabilities, $n(p, \mathbf{r}; t)$, defined on the square lattice with $N=64 \times 64$ (or 128×128) unit cells shown in Fig. 1(a). The function $n(p, \mathbf{r}; t)$ is obtained as a back-Fourier-transform of the solution of the nonlinear equation (32) for $\tilde{n}(p, \mathbf{k}; t)$ at N points \mathbf{k} within the first Brillouin zone. Periodic boundary conditions are used. Since we consider the ordering of an as-quenched disordered state, the initial state is a

disordered state. The disordered state corresponding to the tetragonal T phase is characterized by the function $n(p, \mathbf{r}; 0) = c$, where $c = N_O / 2N = \delta/2$; N_O is the total number of O atoms, and $2N$ is the total number of interstitial sites. We, however, assume that the initial disordered state also includes random "infinitesimal" fluctuations (random noise) and is described by the function $n(p, \mathbf{r}; 0) = c + \delta n(p, \mathbf{r})$, where $\delta n(p, \mathbf{r})$ is the "noise" function obtained by a random-number generator which varies within the range ± 0.001 .

The coordinate and temporal dependence of $n(p, \mathbf{r}; t)$ describes the atomic and mesoscale structure evolution occurring along the transformation path. The short-wave periodic dependence of $n(p, \mathbf{r}; t)$ on \mathbf{r} with the atomic-scale period λ describes the ordered superstructure within this period. Its mesoscale dependence on \mathbf{r} , imposed on the atomic-scale periodic modulation, describes the domain structure of this ordered phase. If the function $n(p, \mathbf{r}; t)$ does not have a short-wave periodic modulation of atomic scale, but depends on the sublattice number p , it describes the orthorhombic O -I ordered phase and the mesoscale distribution of its domains (orientational variants). Local values of the LRO parameter of this phase, η , can be defined as

$$\eta(\mathbf{r}, t) = \frac{n(1, \mathbf{r}; t) - n(2, \mathbf{r}; t)}{2c}. \quad (38)$$

Equation (32) has been formulated in a dimensionless form using the reduced time, $t^* = 4AL_1 t = t/\tau$ [$\tau = (4AL_1)^{-1}$ is the typical diffusion jump time], the reduced temperature, $T^* = k_B T / A$, and the reduced energies expressed in the units of A , where $A = (z^*)^2 \sqrt{2} / a_0$ [see Eq. (20)]. It has been solved with respect to the $2N$ Fourier amplitudes $\bar{n}(p, \mathbf{k}; t)$ using a recurrence formula:

$$\bar{n}(p, \mathbf{k}; t^* + \Delta t^*) = \bar{n}(p, \mathbf{k}; t^*) + \Delta t^* \frac{d\bar{n}(p, \mathbf{k}; t^*)}{dt}, \quad (39)$$

where $d\bar{n}(p, \mathbf{k}; t^*)/dt$ is expressed through $\bar{n}(p, \mathbf{k}; t^*)$ by the right-hand side of (32), and Δt^* is the reduced-time increment. Equation (39) actually relates $\bar{n}(p, \mathbf{k}; t^*)$ and $\bar{n}(p, \mathbf{k}; t^* + \Delta t^*)$. The temporal dependence of $\bar{n}(p, \mathbf{k}; t^*)$ is obtained by applying (39) at consequent moments of time. The choice of the time increment Δt^* was different at high and low temperatures. For example, at $T^* \geq 0.5$ we used $\Delta t^* \sim 10^{-3}$, but for low temperatures we used $\Delta t^* \sim 10^{-4}$. The functions $\tilde{L}_{pq}(\mathbf{k})$, $B_{qs}(\mathbf{k})$, and $V_{qs}^f(\mathbf{k})$ entering (32) are defined by Eqs. (34), (19), and (20), the numerical values (21) and $r_D = 5a_0/\sqrt{2}$ being used. The functions $\tilde{L}_{pq}(\mathbf{k})$, $V_{qs}^f(\mathbf{k})$, and $B_{qs}(\mathbf{k})$ characterize the material properties related to the oxygen diffusion, finite-range O-O interaction, and strain-induced interaction, and, thus, they are not dependent on the oxygen ordering. Because of this, they were calculated only once for all points \mathbf{k} in the first Brillouin zone of the disordered T phase and then were used as the input data array in solving Eq. (32). The latter is the main advantage of the reciprocal-space formalism. Since all interactions are described by the sum of $V_{qs}^f(\mathbf{k})$ and $B_{qs}(\mathbf{k})$, any increase of interaction radius or any modification of potentials just changes these functions, but does not impose any additional computational difficulty.

The set of $2N$ occupation probabilities $n(p, \mathbf{r}; t^*)$, related to the different time moments t^* , describes the temporal evolution of atomic and mesoscale (domain) structure of different ordered states. The graphic visualization of computer-simulation results has been realized by the following way. If the calculated value $n(p, \mathbf{r}; t^*) < c$, the presence of an oxygen atom at the interstice (p, \mathbf{r}) is not shown. If $n(p, \mathbf{r}; t^*) \geq c$, the position of the O atom is shown by the circle placed at the interstice (p, \mathbf{r}) ; the darker the grey level of the circle, the larger the occupation probability $n(p, \mathbf{r}; t^*)$. The resultant microstructural picture obtained in this way imitates the high-resolution electron-microscopic images.

Diffraction effects caused by the oxygen-induced elastic displacements at each time moment t^* have been found by using the elastic displacements $\mathbf{u}(\mathbf{r})$ in Eq. (37). The displacement field, in turn, is determined by Eq. (36), relating it to the distribution functions $n(p, \mathbf{r}; t^*)$ of the O atoms describing the structural transformations. The diffraction pattern found in this way reflects the evolution of both the atomic crystal structure and the domain structure of ordered states. The diffuse intensity visualization is achieved by the white contrast on the black background related to the reciprocal-space areas, where the intensity is negligible.

III. COMPUTER-SIMULATION RESULTS

Our computer simulation has shown that the O-O interaction potential including the long-range repulsive screened-Coulomb and strain-induced interactions, as expected, prevents any decomposition process that would result in the formation of a mixture of completely ordered phases at the ground state. Instead, the phase transformations in this system are congruent ordering reactions that produce local structure inhomogeneities, but maintain a local compositional homogeneity. The concentration dependence of the temperature $T_1 = T_1(c)$ of the primary order-disorder transition $T \rightarrow O$ -I resulting in the O -I orthorhombic phase is described by Eq. (22). The ordering is the second-order transition. The non-stoichiometric primary ordered O -I phase undergoes secondary ordering, which produces the double-period $2a_0 \times a_0$ phase (or O -II phase). The stoichiometric composition for the O -II phase is $\delta = 0.5$ ($\delta = 2c$ is the stoichiometry parameter of $\text{YBa}_2\text{Cu}_3\text{O}_{6+\delta}$). The concentration dependence of the temperature $T_2 = T_2(c)$ of the secondary order-disorder transition O -I \rightarrow O -II resulting in the O -II orthorhombic phase is described by Eq. (24). The O-O interaction energies (19)–(21) entering Eqs. (22) and (24) are chosen so that the calculated $T_1(c)$ and $T_2(c)$ curves are fitted to the observed temperatures at $\delta = 0.5$. Figure 2 shows the T - δ phase diagram calculated with these interaction energies.

A. Computer simulation of tweed and twin pattern formation

1. $T \rightarrow O$ -I ordering

The transformation sequence obtained by the isothermal annealing of a disordered T phase quenched into the O -I stability field proves to be the same at all

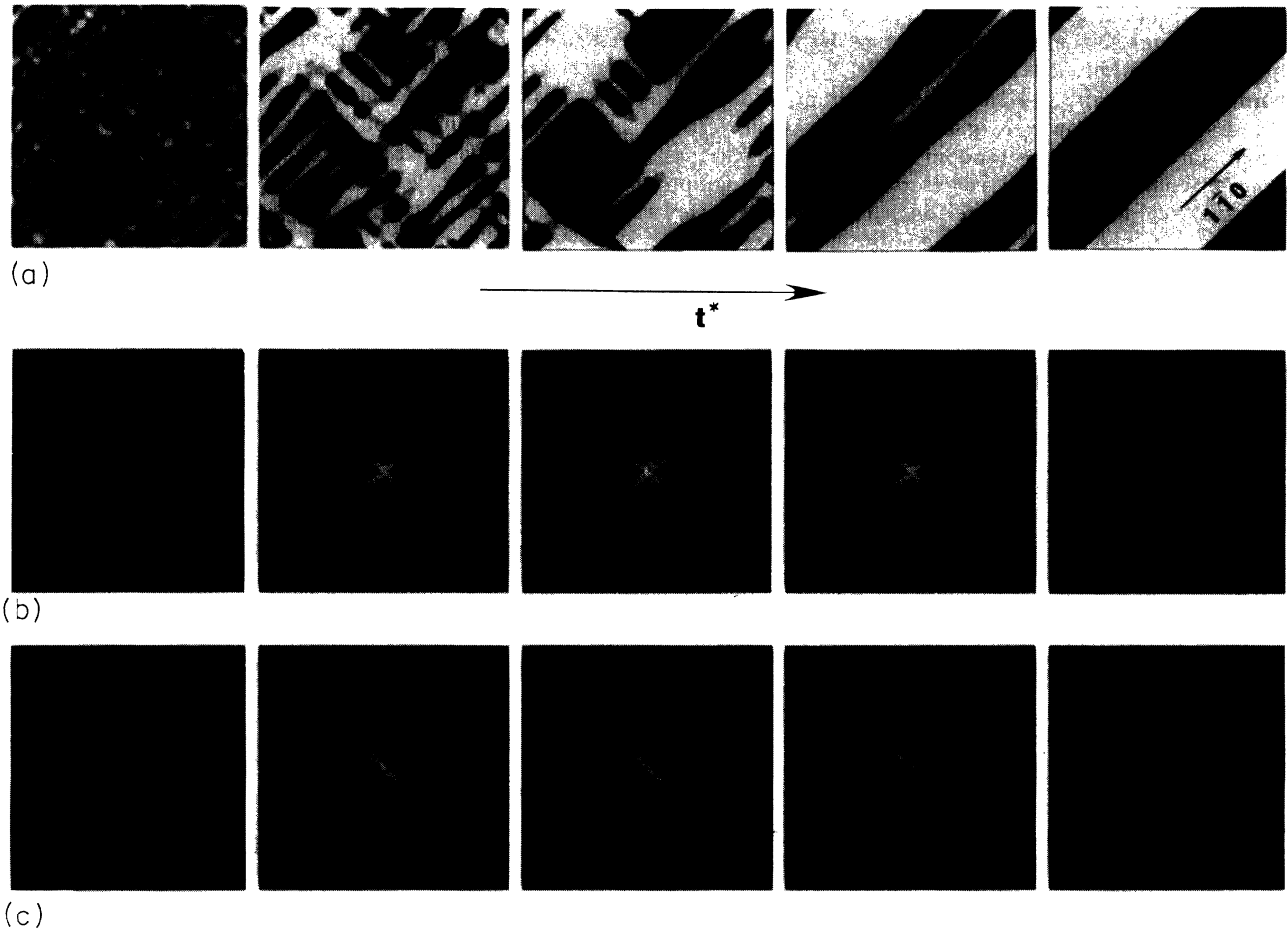


FIG. 3. (a) Simulated temporal isothermal evolution of microstructure in $\text{YBa}_2\text{Cu}_3\text{O}_7$ at the temperature $T/T_1=0.79$. The transformation reduced time t^* is equal to 4, 12, 40, 80, and 120 (from left to right). Two types of orientation domains are characterized by a value of the LRO parameter, $\eta=[n(1,\mathbf{r})-n(2,\mathbf{r})]/2c$ [Eq. (38)]. Regions with positive η describe orientation domains of the first type with preferred occupation of sites of the first interstitial sublattice (light-to-white color). Regions with negative η characterize domains of the second type (black). (b)–(c) are the corresponding strain-induced scattering at $t^*=2.5, 4, 12, 80,$ and 120 (from left to right) around (a) (400) and (b) (440) fundamental diffraction spots. The intensity $I_{\text{stat}}(\mathbf{k})$ [Eq. (37)] is shown on a logarithmic scale. The system size is 128×128 unit cells.

stoichiometries δ . To illustrate the simulation results, we present in Figs. 3–6 typical results for a particular case of the ordering in $\text{YBa}_2\text{Cu}_3\text{O}_7$ ($\delta=1$) at $T/T_1=0.79$. Two orientational variants produced by $T \rightarrow O$ -I ordering are distinguished by the preferentially occupied interstitial sublattice p . According to the definition (38), the LRO parameters in different orientational variants have different signs. The maximum possible value of the LRO parameters is $\eta=1$; the minimum value is $\eta=-1$. In the disordered state, $\eta=0$.

The visualization of calculated structures by the LRO-parameter representation [Fig. 3(a)] is provided by the contrast levels corresponding to the values of η . Areas with negative η are shown by a black background. Areas with $\eta \geq 0$ are shown by different levels: the lighter these levels are, the larger the LRO parameter. Figure 3(a) represents the computer-simulated microstructural evolution within the reduced time range from $t^* \approx 4$ to

$t^* \approx 120$ (at $T/T_1=0.79$). The corresponding evolution of diffuse scattering within the first Brillouin zone around the (400) and (440) diffraction spots is calculated using Eq. (37). It is presented in Figs. 3(b) and 3(c). Figure 3(a) demonstrates that the ordering at $t^* \leq 12$ produces a nanoscale coherent mixture of microdomains of two orientational variants of the O -I phase that are strongly aligned along $\langle 110 \rangle$ directions. The diffuse scattering corresponding to this aligned system of microdomains is characterized by the diffuse streaks along $\langle 110 \rangle$ directions. Both the obtained microstructure and the diffuse scattering are typical for the so-called tweed structure observed in many metal and ceramic systems where the phase transformation develops with point-symmetry reduction.^{53–55} For the $\text{YBa}_2\text{Cu}_3\text{O}_{6+\delta}$ system, the tweed structure was observed in Refs. 22–26.

At $t^*=120$, Fig. 3(a) demonstrates the polytwin structure formed due to tweed pattern coarsening. The corre-

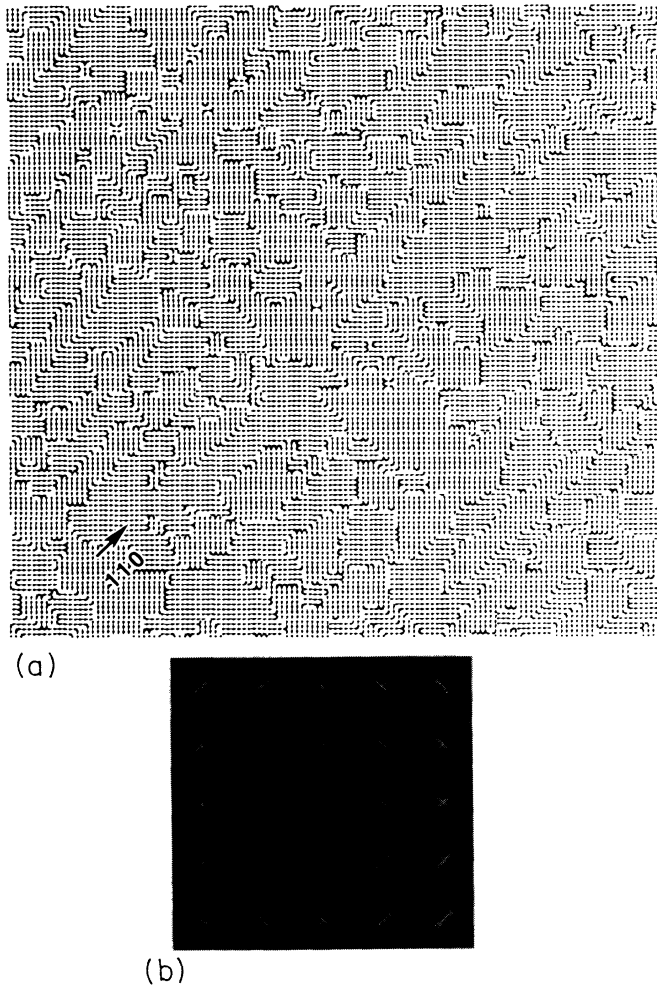


FIG. 4. (a) Atomic representation of the tweed structure in $\text{YBa}_2\text{Cu}_3\text{O}_7$ shown in Fig. 3(a) for $t^*=4$. The small black circles are Cu atoms, and the larger dark circles are O atoms, which are shown if the occupation probability $n(p, \mathbf{r}) > c$ ($c=0.5$ for $\text{YBa}_2\text{Cu}_3\text{O}_7$). (b) The corresponding strain-induced diffuse scattering in the (001) reciprocal-lattice plane from the tweed structure ($t^*=4$). The (000) origin is in the center of the diffraction pattern. Diffuse maxima are around the Bragg peaks. The intensity $I_{\text{stat}}(\mathbf{k})$ [Eq. (37)] is shown on a logarithmic scale. The diffuse maxima are enlarged by the factor 1.6. The model crystal consists of 128×128 unit cells.

sponding diffuse scattering [Figs. 3(b) and 3(c) at $t^*=120$] reveals the streaks caused by the twins' boundaries. These streaks are perpendicular to the (110) twin boundary and parallel to the direction of the diffraction-spot splitting typical for twins. These streaks [Figs. 3(b) and 3(c) at $t^*=120$] obscure the twin-relating splitting of (400) and (440) reflections since the intensity distribution is presented on a logarithmic scale [the splitting is seen in Fig. 5(b), where intensity is presented on the usual, not the logarithmic, scale].

Figure 4(a) shows the "high-resolution" visualization of the atomic structure of the same tweed pattern, which is shown in the "normal-resolution" picture in Fig. 3(a)

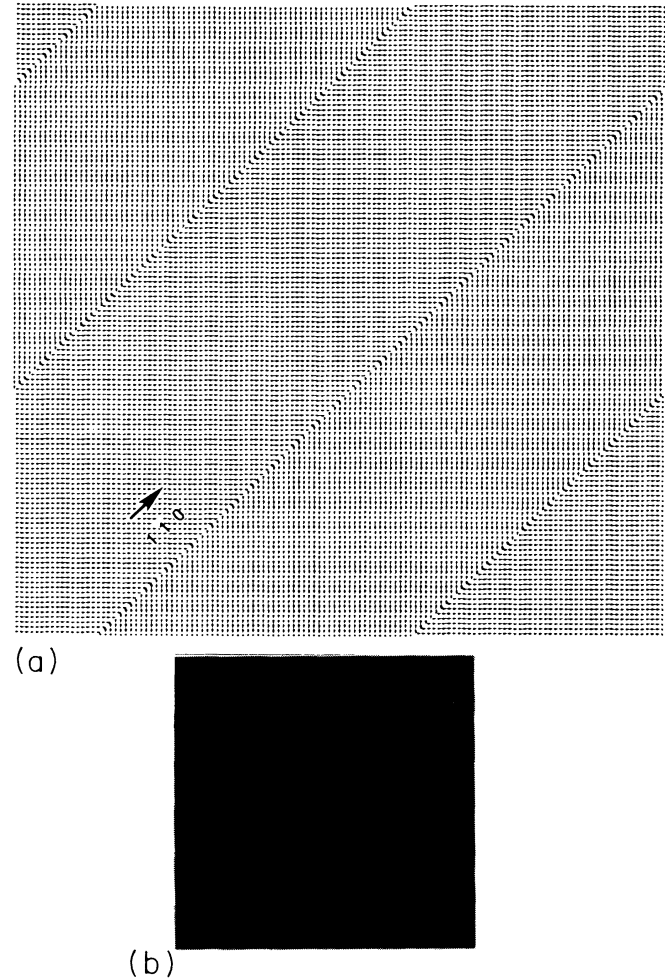


FIG. 5. (a) Atomic representation of the twin structure in $\text{YBa}_2\text{Cu}_3\text{O}_7$ shown in Fig. 3(a) for $t^*=120$. The O atoms are shown if $n(p, \mathbf{r}) > c$ ($c=0.5$). (b) The corresponding diffraction pattern described by the intensity $I(\mathbf{k})_{\text{stat}}$ [Eq. (37)] in the (001) reciprocal-lattice plane. It demonstrates the twin-related splitting of the Bragg peaks. The origin (000) is in the center of the pattern. The diffuse maxima are enlarged by the factor 2.1. Intensities less than 5% of $I(\mathbf{k}=\mathbf{0})_{\text{stat}}$ are not shown. The model crystal consists of 128×128 unit cells.

($t^*=4$). The atomic structure of small orientational domains of the O-I phase aligned along $\langle 110 \rangle$ directions with the preferential boundary orientations along $\langle 110 \rangle$ is clearly seen. Figure 4(b) shows the entire diffraction pattern with the strain-induced diffuse scattering in the (001) reciprocal-lattice plane. It is calculated for the same structure at $t^*=4$. This diffraction pattern, observed in many systems, is a "fingerprint" of the tweed structure.

The "high-resolution" structure of twins formed as a result of the tweed-to-twin diffusional rearrangement is shown in Fig. 5(a) ($t^*=120$). Figure 5(b) gives the corresponding diffraction pattern in the (001) reciprocal-lattice plane [calculated by using Eq. (37)]. The twin-related splitting of diffraction spots, a well-known effect observed practically in all structural studies of $\text{YBa}_2\text{Cu}_3\text{O}_{6+\delta}$, is clearly seen. Both the splitting and the streaks [Figs. 3(b)

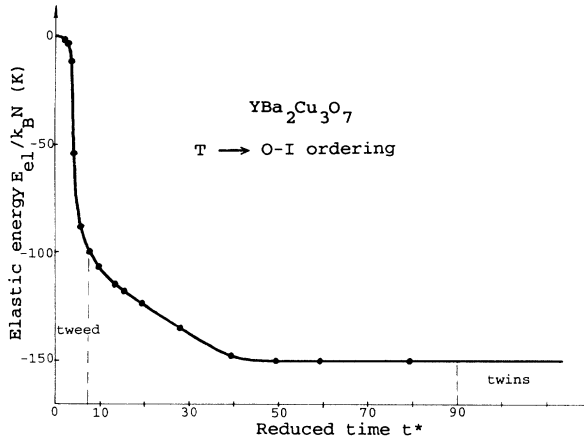


FIG. 6. Temporal evolution of the strain energy at $T \rightarrow O-I$ transformation in $\text{YBa}_2\text{Cu}_3\text{O}_7$ at $T/T_1=0.79$ corresponding to the tweed-to-twin morphology transformation presented in Fig. 3(a). Calculated values are shown by circles. Approximate time intervals corresponding to the tweed and twin patterns are indicated. The disordered state is a reference state.

and 3(c) at $t^*=120$], as expected, are perpendicular to the (110) twin boundary.

At $\delta=1$, besides the temperature $T/T_1=0.79$, the computer simulation has been made for different temperatures within the range $0.54 < T/T_1 < 0.96$. At higher temperatures, close to T_1 , the LRO parameter is very small. Simulation has shown that at $T/T_1=0.96$ the tweed structure is not formed and the structure kinetics directly leads to a polytwin pattern. On the contrary, at lower temperatures ($T/T_1=0.54$) the tweed pattern appears almost immediately, at $t^* \sim 1$, but it takes longer time to transform it into twins.

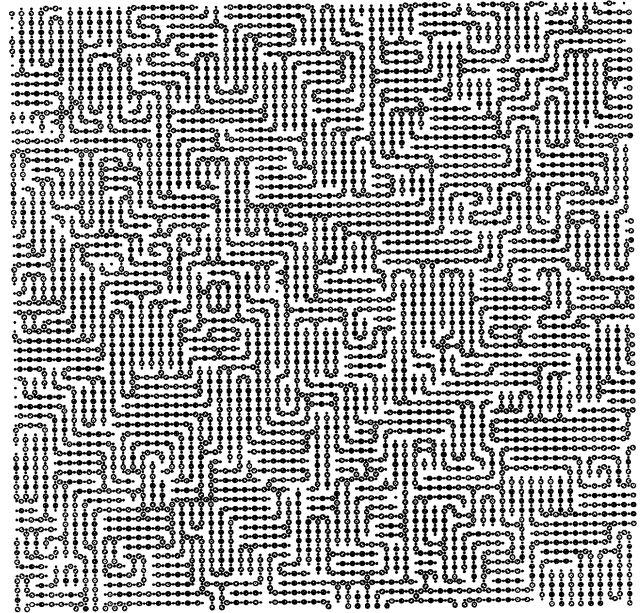
The microstructure evolution, shown in Fig. 3 and resulting in the formation of a polytwin structure through the transient tweed structure, is driven by the strain relaxation. Figure 6 shows the corresponding temporal dependence of the strain energy along the transformation path. An initial disordered state is regarded as the reference state where the strain energy is assumed to be zero. It is interesting that, as follows from this figure, the tweed pattern formation accommodates the major part of the strain energy (about 70% of the reduction of the initial strain energy). The strain energies in Fig. 6 are negative since the initial disordered solution—which is, actually, characterized by the maximum strain energy generated by oxygen-induced displacements—is assumed to be the reference state. Therefore, the strain accommodation caused by the O atoms redistribution reduces the strain energy to negative values.

The computer-simulation results obtained for the stoichiometries $0.25 \leq \delta < 1$ at the temperatures above the $O-II$ field of the phase diagram shown in Fig. 2 prove to be the same as the results obtained at $\delta=1$.

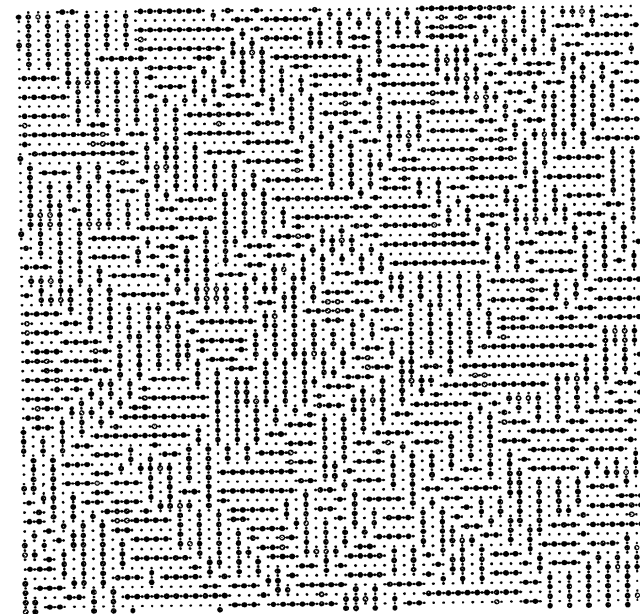
2. $T \rightarrow O-II$ ordering

In this section we present results related to the situation where the disordered T phase is “quenched” into the

$O-II$ field of the phase diagram, i.e., below the $T_2(c)$ line in the congruent phase diagram shown in Fig. 2. The stoichiometries $0.25 \leq \delta \leq 0.85$ were considered. The structure transformations, however, prove to be the same irrespective of the stoichiometry. A disordered T phase



(a)



(b)

FIG. 7. The tweed pattern formation in $\text{YBa}_2\text{Cu}_3\text{O}_{6.5}$ produced by isothermal “annealing” the T phase at $T/T_2=0.72$. (a) the primary tweed consisting of $O-I$ domains (the annealing time $t^*=1.2$), and (b) the secondary tweed consisting of $O-II$ domains formed from the primary tweed domains (the annealing time $t^*=64$). Small black circles are Cu atoms, and larger dark circles are O atoms that are shown if the occupation probability $n(p, \tau) > c$ ($c=0.25$ for $\text{YBa}_2\text{Cu}_3\text{O}_{6.5}$). The model crystal consists of 64×64 unit cells.

“quenched” into the O -II field first undergoes the $T \rightarrow O$ -I ordering producing the tweed pattern similar to that shown in Fig. 4(a). We will call this pattern the primary tweed. Microdomains of the O -I phase forming the primary tweed later transform into the microdomains of O -II phase due to the O -I \rightarrow O -II secondary ordering. The secondary ordering stabilizes the tweed structure, the further evolution of which is halted. This stabilized tweed comprised of O -II domains will be called the secondary tweed. The transformation sequence described above is illustrated by Fig. 7, showing two moments of the structural transformation kinetics in $\text{YBa}_2\text{Cu}_3\text{O}_{6.5}$ at $T/T_2=0.72$, $t^*=1.2$, and $t^*=64$. In the beginning of the evolution, the $T \rightarrow O$ -I ordering produces the primary tweed pattern [Fig. 7(a) for $t^*=1.2$]. It is actually the same pattern as that in Fig. 4(a) for $\text{YBa}_2\text{Cu}_3\text{O}_7$. Figure 7(b) (for $t^*=64$) shows the secondary tweed produced by the O -I \rightarrow O -II ordering within microdomains of the O -I phase. Figure 8 illustrates the evolution of the diffuse scattering around (400) and (440) fundamental reflections. Diffuse scattering is calculated using Eq. (37). The pictures in Fig. 8 include those two generated by the structures shown in Figs. 7(a) and 7(b).

Comparing Figs. 7(a) and 7(b), we do not see any considerable difference between the mesoscale structures of the primary and secondary tweed patterns. The difference can be seen, however, on an atomic scale, where the O -I \rightarrow O -II ordering is manifested. The O -

I \rightarrow O -II ordering is also revealed by the appearance of diffuse maxima around $\{\frac{1}{2}00\}$ points [compare Fig. 8 with Figs. 3(b) and 3(c)]. We have found that the secondary tweed formation, as well as the primary tweed formation, dramatically reduces the strain energy.

An important result is that after $t^* \sim 10$, when the secondary tweed is formed, the transformation kinetics is halted. The observed freezing is a thermodynamic rather than kinetic effect, since it is caused by eliminating the driving force (the diffusional slow-down effect is excluded by measuring the reduced time t^* in the units of the diffusional jump time τ). Therefore, the observed freezing actually means that the system has reached a free-energy local minimum and, thus, is in a metastable state. Therefore, we have arrived at an important conclusion, namely that *the secondary tweed structure is a new kind of the mesoscale phase*. As a metastable phase, the secondary tweed can transform to a conventional equilibrium O -II phase only via the nucleation and growth mechanism.

Our computer simulation has shown that the structure transformations of the T phase at other stoichiometries ($\delta=0.25, 0.6, 0.75$, and 0.85) are the same as the above-described transformations at $\delta=0.5$. This conclusion follows from the results obtained by annealing a disordered $\text{YBa}_2\text{Cu}_3\text{O}_{6+\delta}$ phase “quenched” into the O -II phase field. As in the case $\delta=0.5$, the transformation leads to the metastable secondary tweed formed by the O -I \rightarrow O -II ordering within domains of the transient primary tweed.

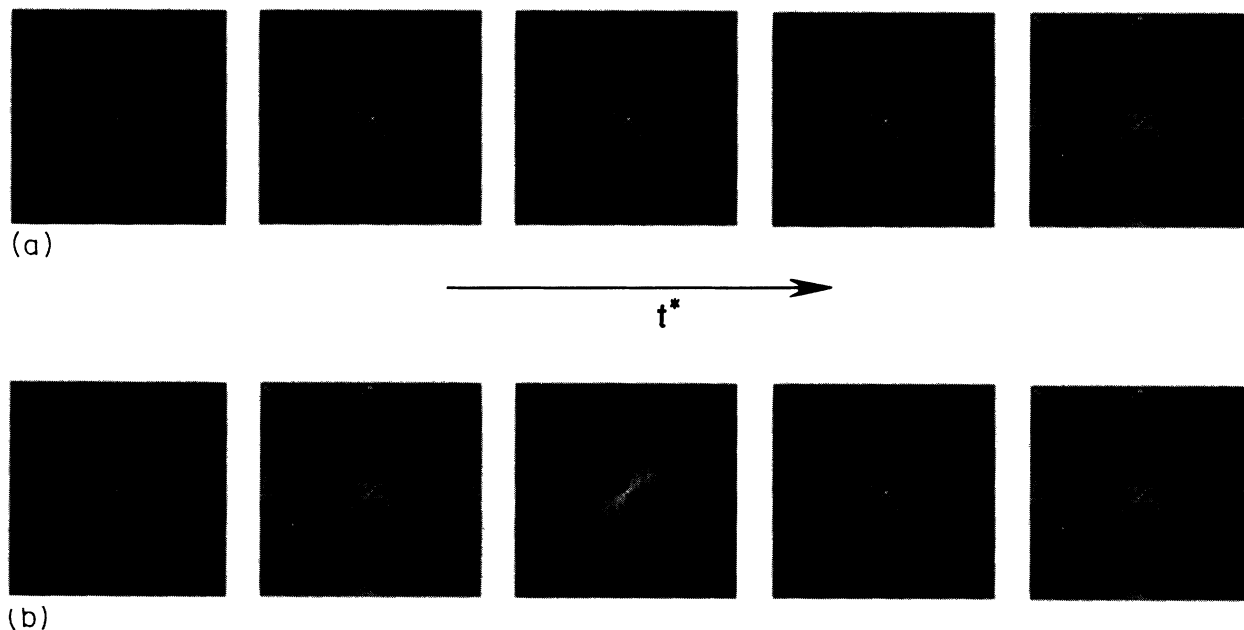


FIG. 8. Evolution of the strain-induced diffuse scattering from $\text{YBa}_2\text{Cu}_3\text{O}_{6.5}$ at the temperature $T/T_2=0.72$. The intensity distribution $I_{\text{stat}}(\mathbf{k})$ (on a logarithmic scale) is shown within the first Brillouin zones with centers in (a) (400) and (b) (440) Bragg maxima. The diffuse maxima are situated in the center of the Brillouin zones. Different states along the transformation path correspond to the reduced times t^* : 0.8, 1.2, 3, 8, and 64 (from left to right). The primary tweed structure is formed at $t^* < 2.5$; the secondary tweed structure appears at $t^* \geq 2.5$. O -I \rightarrow O -II ordering is revealed by appearing the additional $\{\frac{1}{2}00\}$ -type diffuse maxima on the zone boundaries (for $t^*=8$ and 64). The model crystal consists of 64×64 unit cells.

B. Heterogeneous secondary ordering

As follows from the results described in Sec. III A 1, annealing of the T phase within the O -I phase temperature range between $T_1(c)$ and $T_2(c)$ lines on the phase diagram produces a perfect polytwin structure. It takes about 100 reduced-time units ($t^* \sim 30$ – 300 depending on the temperature and size of the system). Therefore, the real-time estimate gives $t \sim 100 \tau$. If the primary ordering temperature $T_1(c)$ is high, which is the case for the high values of the stoichiometry δ , the elementary diffusion time τ should be small and, thus, the polytwin structure consisting of the orientational variants of the O -I phase may have sufficient time to be formed during cooling. Therefore, when the decreasing temperature reaches the secondary ordering temperature $T_2(c)$, the material already has a polytwin structure. Continuing the cooling below the $T_2(c)$ line results in the secondary O -I \rightarrow O -II ordering within the polytwin structure. This is probably always the case if no special effort is made to provide fast cooling (fast quenching produces the secondary tweed structure). To describe the secondary ordering within a polytwin structure during the cooling, we consider a two-step “heat treatment.” The first step, isothermal “annealing” of the T phase at $T_2(c) < T < T_1(c)$, is just intended to obtain a polytwin structure. The second step, the “quenching” of the obtained polytwin structure to below the $T_2(c)$ line and its isothermal “annealing” at $T < T_2(c)$, is intended to study the secondary ordering within the polytwin structure. As will be shown below, the atomic structure of the secondary ordered phases is dramatically affected by the twin morphology.

1. O -I $\rightarrow 2a_0 \times 2a_0 \rightarrow 2a_0 \times a_0$ (O -II) secondary ordering

Figure 9 shows the “high-resolution” pictures of the structures formed in the twinned $\text{YBa}_2\text{Cu}_3\text{O}_{6.5}$. An initial polytwin structure was obtained during the primary $T \rightarrow O$ -I ordering at $T/T_1 = 0.78$ ($t^* = 64$). The secondary ordering is initiated by “quenching” the polytwin structure to the temperature $T/T_2 = 0.63$ and isothermal “annealing” at this temperature. Figures 9(a), 9(b), and 9(c) show three moments of the secondary ordering evolution, $t^* = 32$, $t^* = 64$, and $t^* = 384$. In Fig. 9(a) we mostly see the metastable $2a_0 \times 2a_0$ phase, which is a precursor of the O -II phase, and also several domains of the O -II phase. The volume of the $2a_0 \times 2a_0$ phase decreases as it transforms into the O -II phase [Figs. 9(b) and 9(c)].

As follows from Fig. 9, the (110) twin boundaries change the transformation path. Instead of forming the stable $2a_0 \times a_0$ (O -II) phase, which could be expected from the thermodynamics analysis, the secondary ordering first produces a metastable $2a_0 \times 2a_0$ phase (it was observed in Ref. 5). This phase generates $\{\frac{1}{2} \frac{1}{2} 0\}$ superlattice diffraction maxima. The $2a_0 \times a_0$ phase appears later. It consists of antiphase domains that can be clearly seen in Figs. 9(b) and 9(c). The $2a_0 \times a_0$ phase “inherits” the initial (110) twin orientations. It is interesting that the stable $2a_0 \times a_0$ phase appears from the $2a_0 \times 2a_0$ phase only if the twin boundaries are not perfect. When we occasionally obtained absolutely perfect twin boun-

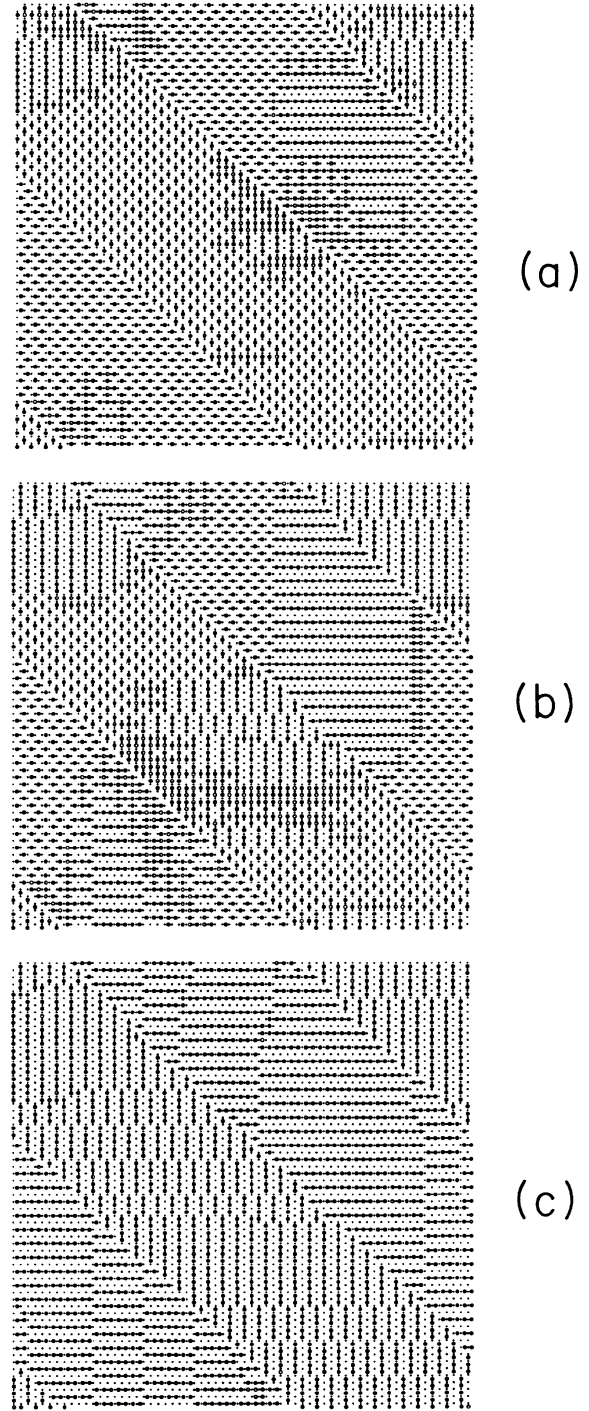


FIG. 9. The transformation of the metastable $2a_0 \times 2a_0$ phase into the stable $2a_0 \times a_0$ (O -II) phase within the O -I twins during the isothermal “annealing” of the O -I phase in $\text{YBa}_2\text{Cu}_3\text{O}_{6.5}$. The initial O -I polytwin structure is formed during the prior “annealing” of the T phase in the O -I field ($T/T_1 = 0.78$, $t^* = 64$). (a), (b), and (c) represent three moments of the evolution at the lower temperature, $T/T_2 = 0.63$, corresponding to the times: $t^* = 32$, 64 , and 384 . The metastable $2a_0 \times 2a_0$ phase forms first. Later it gradually transforms to the O -II phase [(b) and (c)]. The O -II phase forms antiphase domains. If twin boundaries are absolutely perfect, the $2a_0 \times 2a_0 \rightarrow 2a_0 \times a_0$ transformation does not happen. The model crystal consists of 64×64 unit cells.

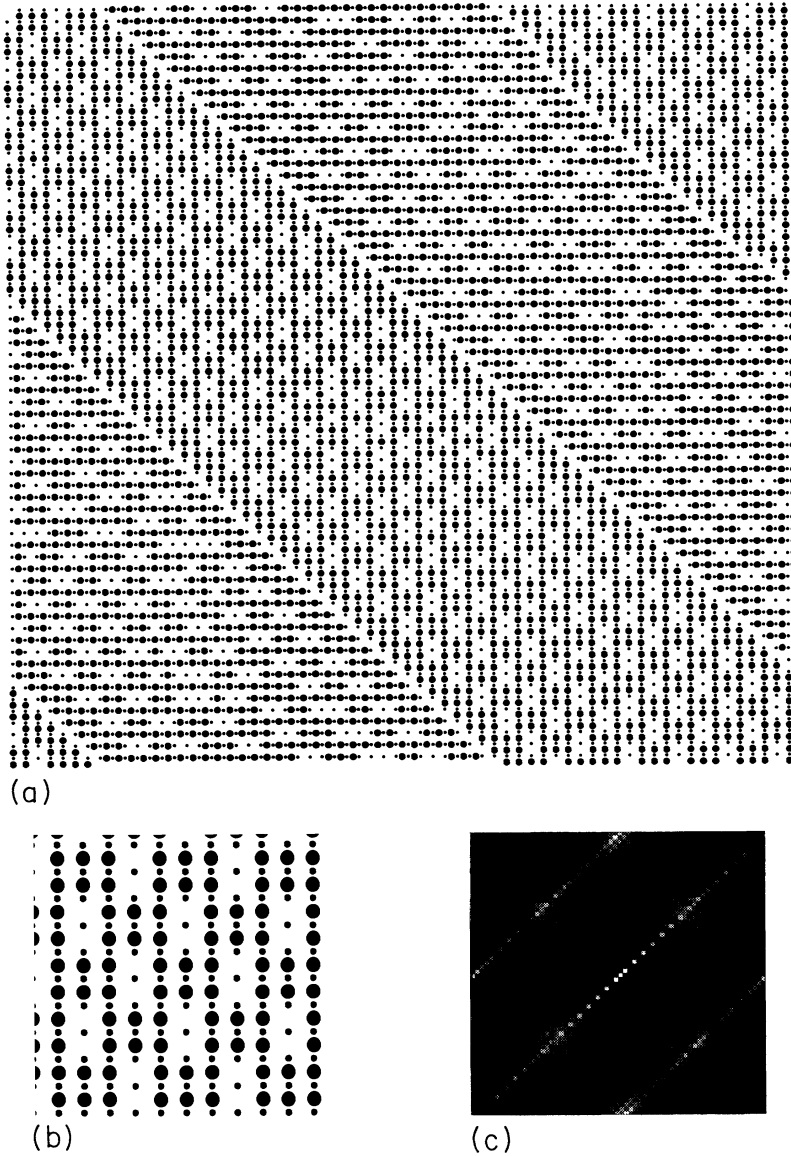


FIG. 10. Simulated *O*-III structure in $\text{YBa}_2\text{Cu}_3\text{O}_{6.75}$. Initial *O*-I polytwinned structure is formed during the high-temperature annealing at $T/T_1=0.78$, $t^*=64$. The following annealings resulting in the secondary and tertiary ordering were at the temperatures $T/T_2=0.61$ ($t^*=128$) and $T/T_2=0.5$ ($t^*=128$). (a) The final tertiary ordered microstructure of the *O*-III ($2\sqrt{2}a_0 \times 2\sqrt{2}a_0$) phase. (b) An enlarged fragment of the structure shown in (a). (c) Intensity distribution within the first Brillouin zone of the $a_0 \times a_0$ host lattice on a logarithmic scale. Four maxima nearest the zone origin are of $\{\frac{1}{4} \frac{1}{4} 0\}$ type, two maxima on the zone boundaries are of $\{\frac{1}{2} 00\}$ type, and streaks along the $\langle 110 \rangle$ directions are generated by twin boundaries. The model crystal consists of 64×64 unit cells.

daries, the $2a_0 \times a_0$ phase did not appear at all.

It is important to note that the same transformation sequence, *O*-I twins $\rightarrow 2a_0 \times 2a_0 \rightarrow$ *O*-II, was obtained not only at $\delta=0.5$, but also at other stoichiometries, varying from $\delta=0.25$ to $\delta=0.85$.

2. *O*-II \rightarrow *O*-III ($2\sqrt{2}a_0 \times 2\sqrt{2}a_0$) tertiary ordering in $\text{YBa}_2\text{Cu}_3\text{O}_{6.25}$, $\text{YBa}_2\text{Cu}_3\text{O}_{6.75}$, and $\text{YBa}_2\text{Cu}_3\text{O}_{6.375}$

When studying the special stoichiometries, $\delta = \frac{1}{4}$, $\frac{3}{8}$, and $\frac{3}{4}$, we found that the *O*-II phase, obtained as described above from a twinned *O*-I phase (i.e., in the sequence *O*-I twins $\rightarrow 2a_0 \times 2a_0 \rightarrow$ *O*-II), undergoes a further transformation if it is annealed at the lower temperature $T < T_3(c) < T_2(c)$ (see Fig. 2). At $T < T_3(c)$ the *O*-II secondary ordered phase transforms to a tertiary ordered *O*-III phase having the $2\sqrt{2}a_0 \times 2\sqrt{2}a_0$ unit cell. Figures

10–12 demonstrate the formation of the *O*-III phase at three different stoichiometries.

Figure 10 presents results for $\text{YBa}_2\text{Cu}_3\text{O}_{6.75}$. A polytwinned *O*-I structure was obtained by “annealing” the *T* phase at $T/T_1=0.78$ ($t^*=64$). The secondary ordering, i.e., the *O*-I $\rightarrow 2a_0 \times 2a_0 \rightarrow$ *O*-II transformation sequence, is achieved by the “annealing” of the polytwinned structure at $T/T_2=0.61$ ($t^*=128$). The tertiary *O*-III phase has appeared as a result of the *O*-II \rightarrow *O*-III transformation at $T/T_2=0.50$ ($t^*=128$). The atomic structure of the *O*-III phase with a $2\sqrt{2}a_0 \times 2\sqrt{2}a_0$ unit cell is more easily seen on Fig. 10(b), showing an enlarged portion of Fig. 10(a). It is orthorhombic and generates the $\{\frac{1}{4} \frac{1}{4} 0\}$ -type superlattice maxima [Fig. 10(c)].

Figure 11(a) presents results for $\text{YBa}_2\text{Cu}_3\text{O}_{6.25}$. The *O*-I polytwins were formed during the “annealing” at $T/T_1=0.83$ ($t^*=64$). The next “annealings” were at $T/T_2=0.72$ ($t^*=128$) and $T/T_2=0.58$ ($t^*=128$).

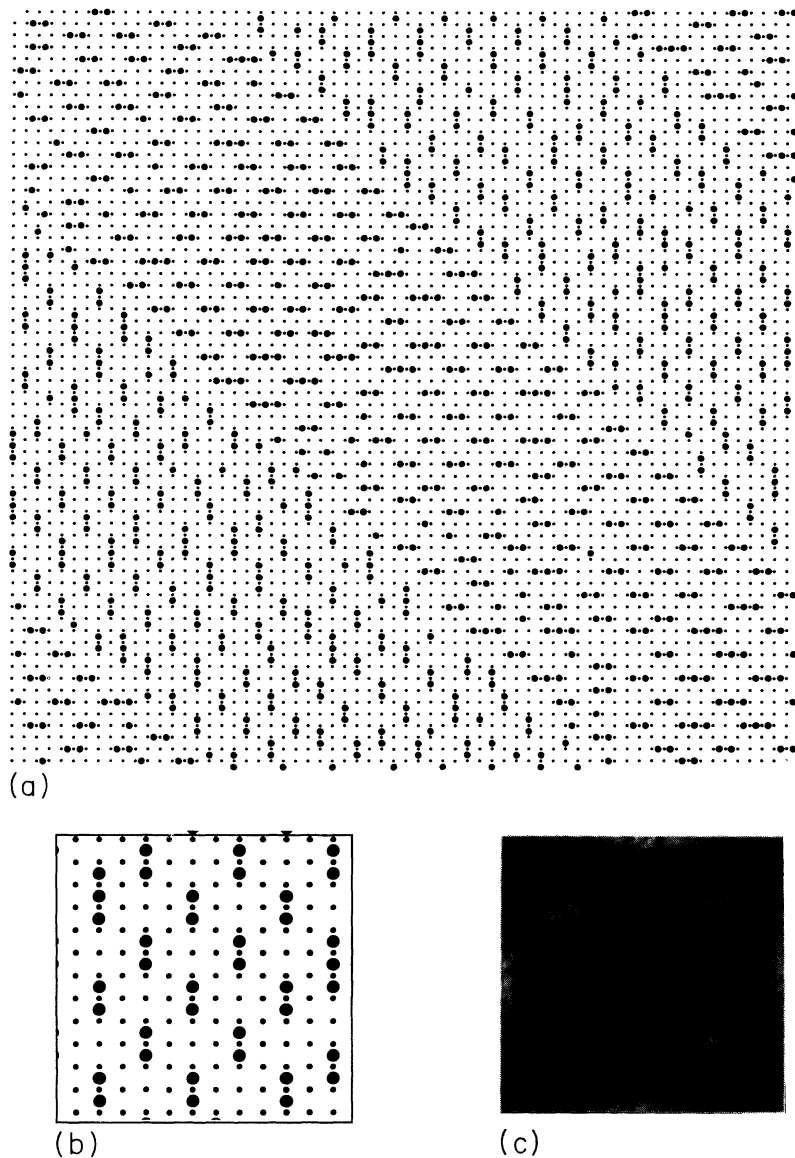


FIG. 11. Simulated *O*-III structure in $\text{YBa}_2\text{Cu}_3\text{O}_{6.25}$. Initial *O*-I polytwinned structure is formed during the high-temperature annealing at $T/T_1=0.83$, $t^*=64$. The following annealings resulting in the secondary and tertiary ordering were at the temperatures $T/T_2=0.72$ ($t^*=128$) and $T/T_2=0.58$ ($t^*=128$). (a) The final tertiary ordered microstructure of the *O*-III ($2\sqrt{2}a_0 \times 2\sqrt{2}a_0$) phase. (b) An enlarged fragment of the structure shown in (a). (c) Intensity distribution within the first Brillouin zone of the $a_0 \times a_0$ host lattice on a logarithmic scale. Four maxima nearest the zone origin are of $\{\frac{1}{4} \frac{1}{4} 0\}$ type, four maxima on the zone boundaries are of $\{\frac{1}{2} 0 0\}$ type, and streaks along the $\langle 110 \rangle$ directions are generated by twin boundaries. The model crystal consists of 64×64 unit cells.

This steplike “annealing” imitates a slow-cooling procedure. The crystallographic structure of the *O*-III phase also has the $2\sqrt{2}a_0 \times 2\sqrt{2}a_0$ unit cell [a part of Fig. 11(a) is shown in Fig. 11(b)]. It is actually anti-isomorphic to the *O*-III structure in $\text{YBa}_2\text{Cu}_3\text{O}_{6.75}$ [Fig. 10(b)]: each one can be obtained from the other by the substitution of O atoms for vacancies and vice versa. The structure is also orthorhombic and generates the same $\{\frac{1}{4} \frac{1}{4} 0\}$ -type superlattice maxima [Fig. 11(c)].

Figure 12 presents results for $\text{YBa}_2\text{Cu}_3\text{O}_{6.375}$. This stoichiometry is chosen since it is close to that ($\delta=0.35$) investigated in the recent neutron-diffraction study.⁹ The initial polytwinned *O*-I structure has been formed at $T/T_1=0.84$ ($t^*=64$). The next “annealings,” imitating slow cooling, were as follows: at $T/T_2=0.75$ ($t^*=32$),

then the “annealing” at $T/T_2=0.42$ ($t^*=128$), and then the “annealing” at $T/T_2=0.32$ ($t^*=128$). A portion of Fig. 12(a) is shown in Fig. 12(b). The *O*-III phase also has the $2\sqrt{2}a_0 \times 2\sqrt{2}a_0$ unit cell, but its atomic arrangement is different than those shown in Figs. 10(b) and 11(b) and also different than structure proposed in Ref. 9. The diffraction pattern is presented in Fig. 12(c). It also displays $\{\frac{1}{4} \frac{1}{4} 0\}$ -type superlattice maxima.

The superstructure maxima of $\{\frac{1}{4} \frac{1}{4} 0\}$ type were observed in Refs. 5 and 7–9; an electron-microscopic image of the *O*-III phase is presented in Ref. 5.

The *O*-III phase unit cells [easily seen in Figs. 11(b), 12(b), and 10(b)] are formed by different numbers of oxygen atoms, namely, two, three, and six (or two oxygen vacancies), which is dictated by the stoichiometries $\delta = \frac{2}{8}, \frac{3}{8}, \frac{6}{8}$,

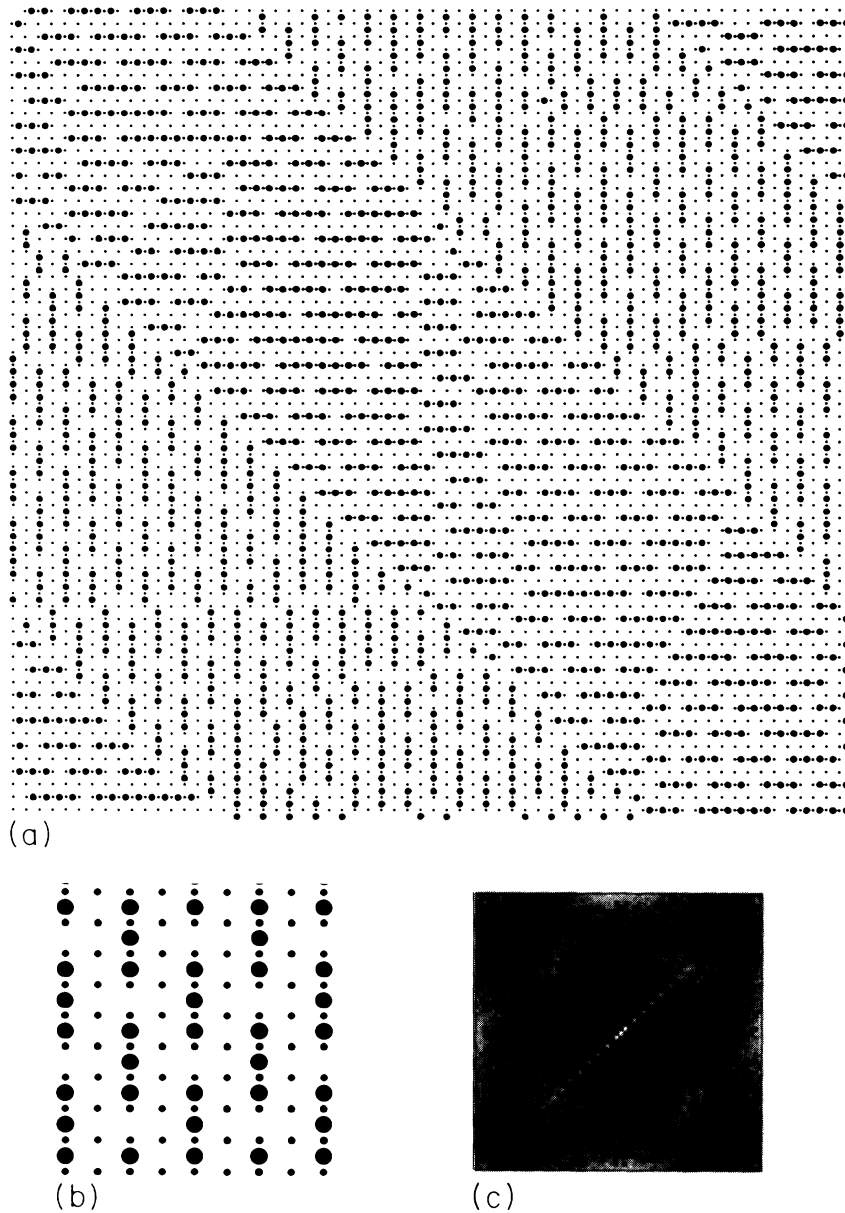


FIG. 12. Simulated *O*-III structure in $\text{YBa}_2\text{Cu}_3\text{O}_{6.375}$ ($\delta = \frac{3}{8}$). Initial *O*-I polytwinned structure was formed during the high-temperature annealing at $T/T_1 = 0.84$, $t^* = 64$. The next annealings resulting in the secondary and tertiary ordering were at the temperatures $T/T_2 = 0.75$ ($t^* = 32$), $T/T_2 = 0.42$ ($t^* = 128$), and $T/T_2 = 0.32$ ($t^* = 128$). (a) The final tertiary ordered microstructure of the *O*-III ($2\sqrt{2}a_0 \times 2\sqrt{2}a_0$) phase. (b) An enlarged fragment of the structure shown in (a). (c) Intensity distribution within the first Brillouin zone of the $a_0 \times a_0$ host lattice on a logarithmic scale. Four maxima nearest the zone origin are of $\{\frac{1}{4}, \frac{1}{4}, 0\}$ type, four maxima on the zone boundaries are of $\{\frac{1}{2}, 0, 0\}$ type, and streaks along the $\langle 110 \rangle$ directions are generated by twin boundaries. The model crystal consists of 64×64 unit cells.

and $\frac{6}{8}$, respectively. Being a tertiary ordered phase based on the *O*-II parent structure, the *O*-III phase also generates $\{\frac{1}{2}, 0, 0\}$ superlattice maxima. They are situated on the Brillouin-zone boundaries [Figs. 10(c), 11(c), and 12(c)].

3. Homogeneous secondary ordering

Computer-simulation results presented earlier have demonstrated that the (110) accommodation twins affect the secondary and tertiary ordering. They lead to the heterogeneous ordering that promotes the concentration waves whose wave vectors are perpendicular to the twin plane. Indeed, the computer-simulated structures ($2a_0 \times 2a_0$) and the *O*-III phases shown in Figs. 9–12 are

generated by the concentration waves with wave vectors $(2\pi/a_0)(\frac{1}{2}, \frac{1}{2}, 0)$ and $(2\pi/a_0)(\frac{1}{4}, \frac{1}{4}, 0)$, which are perpendicular to the (110) twin plane. Therefore, to investigate the secondary ordering that is not influenced by the twin boundaries, we either have to consider a very large system, which is impractical since it requires overly large computational times, or to consider the secondary ordering in a single orientational domain of the *O*-I phase. Computer-simulation results for the latter case are presented below.

Figure 13 shows typical microstructures obtained during the isothermal secondary ordering of the *O*-I phase at $T < T_2$ (c) at the stoichiometries $\delta = 0.25, 0.5, 0.55, 0.6,$ and 0.85 (all of the pictures in Fig. 13 display only one-quarter of the 120×120 computational cell). A single

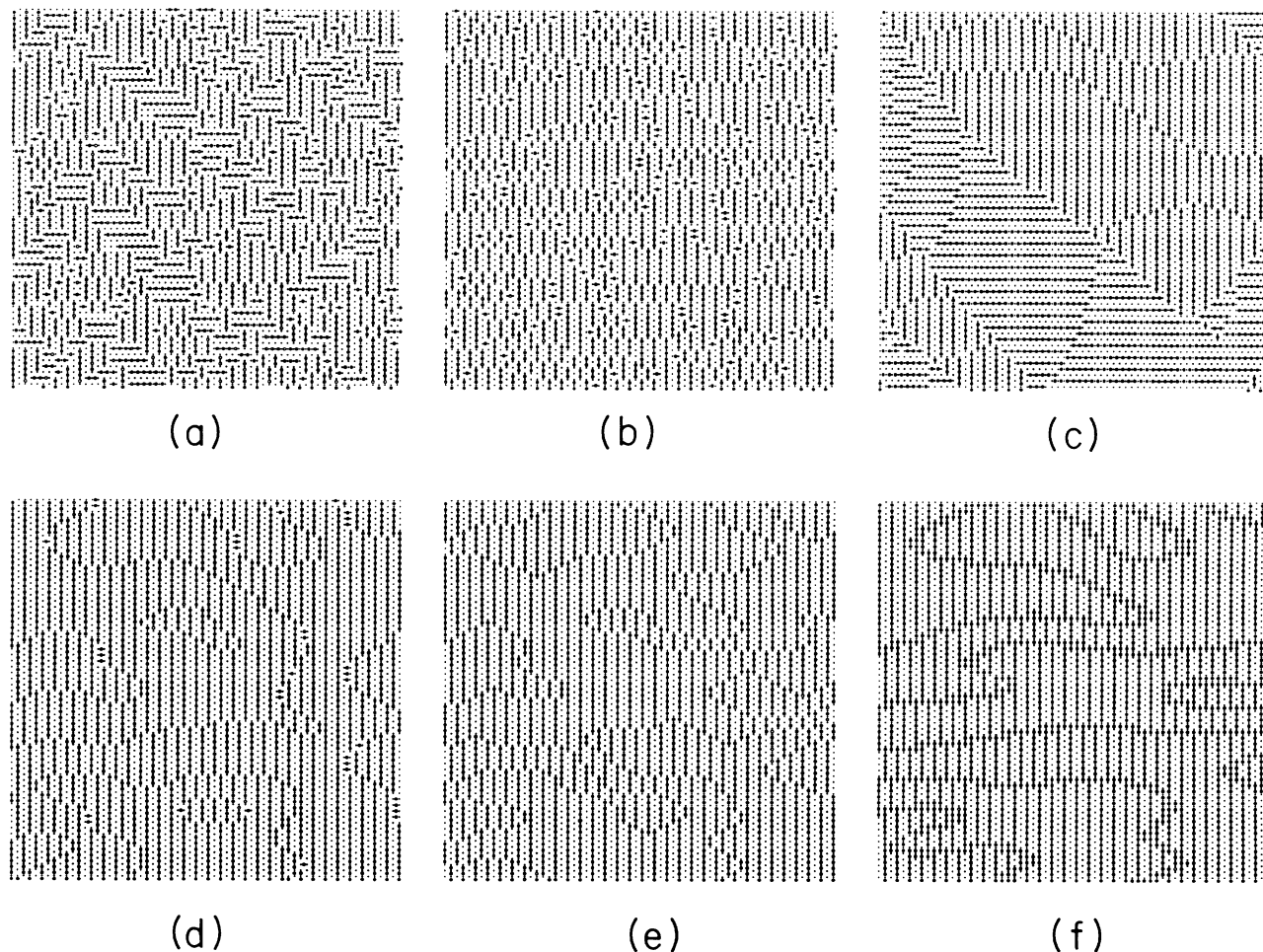


FIG. 13. Microstructures obtained by isothermal homogeneous secondary ordering of a single orientational variant of the *O-I* phase at the room temperature. Microstructures (a)–(f) are obtained by the following “heat treatments”: (a) $\delta=0.25$, $T=T_{\text{room}}(t^*=160)$; (b) $\delta=0.5$, $T=T_{\text{room}}(t^*=80)$; (c) $\delta=0.5$, $T/T_2=0.95$ ($t^*=80$) plus $T/T_2=0.9$ ($t^*=40$) plus $T=T_{\text{room}}$ ($t^*=160$); (d) $\delta=0.55$, $T/T_2=0.95$ ($t^*=40$) plus $T=T_{\text{room}}$ ($t^*=80$); (e) $\delta=0.6$, $T=T_{\text{room}}$ ($t^*=80$); (f) $\delta=0.85$, $T=T_{\text{room}}$ ($t^*=80$). Microstructure (a) ($\delta=0.25$) corresponds to the secondary tweed. Microstructure (c) ($\delta=0.5$) obtained by the steplike cooling shows large domains of the *O-II* phase. Microstructures (b) and (d)–(f) ($\delta=0.5$ – 0.85 , respectively) describe a metastable “glassy” phase (SRO of *O-II* type). At $\delta=0.85$, (f), the O atoms are shown if $n(p,r) \geq \delta$. The model crystal consists of 120×120 unit cells, but only one-quarter of the computational cell is shown.

orientational variant of the *O-I* phase with infinitesimal fluctuations of occupation probabilities was considered an initial state ($t^*=0$). All microstructures presented in Fig. 13 are obtained either by quenching or cooling the initial state to room temperature, T_{room} . The cooling, embodied by the two cases depicted in Figs. 13(c) and 13(d), was imitated by a steplike isothermal annealing at the higher temperatures T [$T_{\text{room}} < T < T_2(c)$] and subsequent isothermal annealing at the room temperature (during the time $t^*=80$ or 160). Figures 13(a), 13(b), 13(e), and 13(f) show the structures obtained by the direct quenching (plus “annealing”) to room temperature.

Figures 13(b) and 13(c) allow us to compare the microstructures obtained for the same stoichiometry, $\delta=0.5$, by “quenching” and “slow cooling” to $T=T_{\text{room}}$. The “quenching” [Fig. 13(b)] produces pieces of parallel *O-Cu-O*- chains with the same orientation as the chains of the initial *O-I* domain. A number of oxygen atoms have

moved to “wrong” interstitial sites, which are forbidden in both the *O-I* and *O-II* phases. The “slow cooling” of the same system, $\delta=0.5$ [Fig. 13(c)], was achieved by the three-step annealing—at $T/T_2=0.95$ during $t^*=80$, then at $T/T_2=0.9$ during $t^*=40$, and then at $T=T_{\text{room}}$ during $t^*=160$. As follows from Fig. 13(c), this treatment transforms a single *O-I* domain into the (110) twins of the *O-II* phase, the twin components being filled by the antiphase domains of the *O-II* phase. The size of the antiphase domains is of the order of the twin size.

An unexpected result is that at stoichiometries above $\delta \sim 0.5$ the final microstructure is not affected by the “heat-treatment” regime. Both “slow cooling” and “quenching” produces the same type of microstructure. The stoichiometry of the system affects only the antiphase-domain boundary structure [compare the structures shown in Fig. 13(d) for $\delta=0.55$, Fig. 13(e) for $\delta=0.6$, and Fig. 13(f) for $\delta=0.85$].

The structures with stoichiometry $\delta > 0.5$, shown in Figs. 13(d)–13(f), consist of the antiphase domains of the *O*-II phase. The antiphase boundaries terminate -O-Cu-O- chains parallel to the *b* axis whose length is determined by the antiphase-domain size. The coherent mixture of these antiphase domains can be interpreted as a realization of the $(\frac{1}{2}00)$ short-range order in the *O*-I phase since wide diffuse maxima at the $\{\frac{1}{2}00\}$ points correspond to the *O*-II short-range order. These structures are metastable or stable since they stop to evolve at $t^* \sim 40$ –100 (this t^* depends on the temperature). The structure presented in Figs. 13(d)–13(f) can be interpreted as a “glassy” state since in many respects it is similar to an amorphous or spin-glass state. The O atoms on Fig. 13(f) are shown if $n(p, \mathbf{r}) \geq \delta(2c) = 0.85$, where $\delta = 0.85$ is equal to the occupation probability $n(p, \mathbf{r})$ of finding an oxygen atom in the occupied sublattice of a “disordered” *O*-I phase (the occupation probability in the other sublattice of the *O*-I phase is practically zero). The *O*-I \rightarrow *O*-II ordering just imposes a modulation around the value δ . In all other figures presented in this work, O atoms are shown if $n(p, \mathbf{r}) \geq c$.

At $\delta < 0.5$ the room-temperature “annealing” of a single *O*-I domain quenched to room temperature produces structures different from those obtained at $\delta > 0.5$. The room-temperature secondary ordering at $\delta < 0.5$ produces a mixture of two orientational variants of the *O*-II phase. This effect is illustrated in Fig. 13(a) ($\delta = 0.25$). The structure shown in Fig. 13(a) practically coincides with the secondary tweed structure obtained by direct $T \rightarrow$ *O*-II quenching [compare with Fig. 7(b)]. It also generates strain-related diffuse scattering around the fundamental reflections similar to that found for the secondary tweed pattern [Fig. 8, $t^* \geq 2.5$].

Therefore, the exact stoichiometry of the *O*-II phase, $\delta = 0.5$, separates two structural areas formed by the homogeneous secondary ordering: the secondary tweed area and the “glassy” state area. All these structures shown in Figs. 13(a)–13(f) [as well as that presented in Fig. 7(b)] are metastable or stable since they halt to evolve at $t^* \sim 100$.

IV. DISCUSSION

We may expect that the long-range Coulomb or screened-Coulomb repulsion between oxygen ions suppresses the decomposition since the segregation of ions of the same sign, required by any decomposition, is “penalized” by a dramatic increase in the electrostatic energy. The larger the segregation size, the greater the electrostatic energy. This effect should prevent the coarsening that produces macroscopic domains of the product phases with different compositions and, thus, is an integral part of any decomposition process. Under these circumstances, the congruent ordering is the only possible type of phase transformation. In this case, the atomic structure of an ordered state has to adjust to the current composition to make it stoichiometric. It has been shown above that, depending on the stoichiometry and the heat treatment, the ordered state may be one of the conventional single-phase superstructures, *O*-I, *O*-II,

$2\sqrt{2}a_0 \times 2\sqrt{2}a_0$ (*O*-III), and the $2a_0 \times 2a_0$ transient phase. We have also found that the long-range interaction results in new kinds of metastable (or stable) phases, namely the secondary tweed and “glassy”-type phases, which we call the mesoscopic phases. Although the mesoscopic phases cannot be distinguished from conventional phases thermodynamically, their crystallographic structure is substantially different. They are characterized by mesoscale rather than by atomic-scale structure. The local oxygen composition for all these structures is homogeneous across the sample.

Our computer simulation describes the transformation kinetics at all temperatures in terms of the dimensionless time t^* . Using the reduced time t^* enables us to exclude the effect of diffusional “freezing.” Measuring the reduced time t^* in units of τ , the typical time of an elementary diffusion event, translates the diffusional “freezing” into increasing the time unit τ and, thus, to rescaling a reduced time t^* . Therefore, the computer-simulation results reflect the effect of the thermodynamic driving force on the kinetics. However, the diffusional “freezing” affects, of course, the real-time evolution. To find the temperature range of applicability of our computer-simulation results, we have to estimate the typical diffusion time τ , which relates the reduced time t^* and the real time t according to the equation $t^* = 4L_1 At = t/\tau$. Knowing τ , we would be able to estimate the lowest temperature at which the kinetic processes simulated in our study could still be detected during the realistic interval of the real time. We would be also able to estimate the highest temperature allowing us to fix by quenching the high-temperature state.

The diffusional time τ can be estimated by using the oxygen diffusion coefficient D_{ab} in the (001) Cu-O plane containing the *a* and *b* axes. A simple estimate gives

$$\tau \sim a_0^2 / 4D_{ab} .$$

Measurements of the tracer diffusion of oxygen in $\text{YBa}_2\text{Cu}_3\text{O}_{7-\delta}$ polycrystals by Rothman *et al.*⁵⁶ gives

$$D_{\text{poly}} \sim (1.4 \times 10^{-4}) \exp \left[-\frac{0.97 \text{ eV}}{k_B T} \right] \text{ cm}^2 \text{ s}^{-1} .$$

Since the diffusion coefficient in the *c* direction is $\sim 10^6$ times lower than that in the *a*-*b* plane,⁴⁷ the diffusion along the *c* axis can be neglected. Then, $D_{ab} \approx D_{\text{poly}}$. With $a_0 \approx 3.86 \times 10^{-8}$ cm, we obtain the following estimate for the time-scale unit τ :

$$\tau \sim (2.7 \times 10^{-12}) \exp \left[\frac{0.97 \text{ eV}}{k_B T} \right] \text{ s} . \quad (40)$$

According to this estimate, the typical diffusion jump time at the room temperature is equal to $\tau_{\text{room}} \sim 8.9 \times 10^4$ s ~ 24 h. This estimate shows that our computer simulation of the ordering kinetics can be applied, at least, down to the room temperature, where the diffusion kinetics of ordering is still not frozen. This conclusion coincides with the observation of the diffusion ordering kinetics at the room temperature.⁵⁷

The computer-simulation results demonstrate that the

structural kinetics and the structures ultimately obtained in $\text{YBa}_2\text{Cu}_3\text{O}_{6+\delta}$ are strongly dependent on the thermal history of a sample. The main simulation results are as follows.

A. Stoichiometries below $\delta \sim 0.5$

The $T \rightarrow O\text{-II}$ quenching (from the T field into the $O\text{-II}$ field of the phase diagram) always produces the secondary tweed structure consisting of twin-related microdomains of the $O\text{-II}$ phase with the $\langle 110 \rangle$ alignment [Fig. 7(b)]. However, the real-time estimate [Eq. (40)] indicates that the quenching of the T phase into the $O\text{-II}$ field is hardly technically possible at $\delta > 0.5$. The maximum achievable quenching rate within this range is not sufficiently high to prevent the primary $T \rightarrow O\text{-I}$ ordering during the quenching, since within this composition range the temperature $T_1(c)$ and, thus, the diffusion rate is too high. Therefore, the secondary tweed could be obtained by the $T \rightarrow O\text{-II}$ quenching only within the composition range of the $O\text{-II}$ phase below a stoichiometry $\delta \sim 0.5$. At room temperature this range, according to our phase diagram (Fig. 2), is $\sim 0.17 \leq \delta < \sim 0.5$.

The powder-diffraction pattern generated by the secondary tweed cannot be distinguished from that of the tetragonal phase of the same composition. However, the secondary tweed can be identified on a single-crystal diffraction pattern, which is predicted to be characterized by the strain-related diffuse maxima around the Bragg peaks. These maxima are streaks or crosses elongated in the $\langle 110 \rangle$ directions (Fig. 8). It is much more difficult to observe the predicted diffuse maxima around $\{\frac{1}{2}00\}$ points caused by the $O\text{-II}$ order in the secondary tweed. There are two reasons for this. The first is that these maxima are generated by direct scattering by O atoms in ultrafine domains of the $O\text{-II}$ phase forming the tweed. The second is that the oxygen content is small within the range $\sim 0.17 \leq \delta < \sim 0.5$ where the secondary tweed is formed.

It should be emphasized that the $T \rightarrow O\text{-II}$ quenching is not the only predicted mechanism of secondary tweed formation. Another mechanism is a homogeneous $O\text{-I} \rightarrow O\text{-II}$ secondary ordering within macroscopically large domains of the $O\text{-I}$ phase. It is shown in this study that this mechanism is operative within the same composition range as the $T \rightarrow O\text{-II}$ quenching mechanism, viz., at stoichiometries below $\delta \sim 0.5$. The secondary ordering within this range produces twin-related microdomains of the $O\text{-II}$ phase arranged into the tweed microstructure aligned along the $\langle 110 \rangle$ directions [Fig. 13(a)]. The secondary tweed structures shown in Figs. 13(a) and 7(b), as well as their diffraction patterns, are indistinguishable.

Our computer simulation has demonstrated that the secondary tweed obtained by both mechanisms is a mesoscopic phase. This phase is metastable because it corresponds to the free-energy local minimum. Unlike conventional phases, it is identified by a mesoscale rather than an atomic-scale structure and is stabilized by the strain-induced and Coulombic long-range interactions. The formation of the secondary tweed below $\delta \sim 0.5$ during the secondary ordering of the $O\text{-I}$ phase leads to an interesting prediction. The prediction concerns a behav-

ior of the secondary tweed, obtained from a macroscopically coarse $O\text{-I}$ polytwin structure, in a heating-cooling cycle. Heating the secondary tweed into the $O\text{-I}$ field should result in its disappearance and, thus, in a restoration of the initial polytwin structure consisting of domains of the $O\text{-I}$ phase. As follows from our computer simulation results, the cooling of this structure back to the $O\text{-II}$ field should restore the secondary tweed. Therefore, the appearance of the secondary tweed is a reversible phenomenon.

The primary tweed has a different nature. It is a transient mesoscale structure which appears as a precursor to the stable (110) polytwin structure during the primary $T \rightarrow O\text{-I}$ ordering. It is not metastable and, thus, cannot be regarded as a mesophase. The primary tweed formation and its arrangement into a polytwin structure are illustrated by Fig. 3. The typical "high-resolution" structure and diffraction pattern of the primary tweed are shown in Fig. 4.

The primary and secondary tweed formation are driven by the strain accommodation. For example, as follows from Fig. 6, an occurrence of the primary transient tweed reduces the strain energy by about 70%. The following strain accommodation, predicted by the computer simulation, yields the $O\text{-I}$ phase polytwin structure [Fig. 5(a)]. We have found that the twin boundaries are oxygen-depleted (the visualization method employed does not always clearly display this effect). The larger the stoichiometry deviation from $\delta = 1$, the greater the depletion effect.

A simulated diffraction pattern generated by the obtained polytwin structure shows a splitting of Bragg spots in the $\langle 110 \rangle$ directions, normal to the twin boundary [Fig. 5(b)]. According to the conventional explanation of this effect in real materials, the splitting is caused by the mutual rotation of the twin-related variants required to provide the crystal-lattice continuity across the twin boundary, the rotation angle, and, thus, the splitting being expressed in terms of the crystal-lattice parameters. Our theoretical formulation [Eqs. (36) and (37)] actually suggests a more general approach. It presents both the twin splitting of the Bragg peaks and the tweed-related diffuse scattering, as a result of the diffraction effect caused by a superposition of displacement fields generated by interstitial oxygen atoms.

The predictions of the theory seem to be in an agreement with electron-microscopic observations. According to Zhu *et al.*,²⁵ the tweed structure in pure $\text{YBa}_2\text{Cu}_3\text{O}_{6+\delta}$ is observed only in strongly nonstoichiometric oxides. It has been observed, in particular, in $\text{YBa}_2\text{Cu}_3\text{O}_{6.23}$. Since this tweed pattern does not evolve into a twin pattern, the structure is probably a secondary tweed, although the diffuse scattering around $\{\frac{1}{2}00\}$ points has not been detected. The latter fact is not, however, surprising under conditions of a small oxygen content and the ultrafine size of ordered microdomains. Electron-microscopic pictures and microdiffractograms of the tweed structure obtained by Xu and co-workers²³ and Zhu and co-workers^{25,26} are in very good agreement with the simulated structures and diffraction patterns shown in Figs. 7 and 8.

The predicted primary-tweed-to-polytwin rearrangement (Fig. 3) is also supported by experimental studies. The observations of Amelinckx *et al.*,²² illustrated by *in situ* made video,⁵⁸ have demonstrated how a tweed pattern appears at high temperatures upon cooling and later rearranges into a polytwin pattern. This kinetic behavior and the observed structures are very similar to those predicted by our computer simulation for the primary-tweed-to-twin evolution [Figs. 3(a), 4(a), and 5(a)]. The tweed diffraction pattern and its evolution to a polytwin-induced pattern observed in Ref. 22 also coincide with the theoretical predictions [Figs. 3(c), 3(b), 4(b), and 5(b)]. The diffraction patterns of the primary tweed and the secondary tweed practically coincide [compare Figs. 3(b), 3(c), and 8]. In general, we could say that the observed tweed patterns and the shape of the diffuse scattering around the fundamental reflections reported in Refs. 22–26 are in striking agreement with the computer-simulation results shown in Figs. 3–8. It is noteworthy that our simulation has revealed the generic properties of a tweed structure, common for systems of a very different nature. The structures and diffraction effects, simulated for a specific case of $\text{YBa}_2\text{Cu}_3\text{O}_{6+\delta}$, are similar to those observed in other systems.^{53–55,59}

B. Stoichiometries above $\delta \sim 0.5$

On the other side of the composition range—that is, above stoichiometry $\delta \sim 0.5$ —the $T \rightarrow O\text{-I}$ ordering temperature $T_1(c)$ is comparatively high (see Fig. 2) and thus, the diffusion rate in this area is very high. The real-time estimate [Eq. (40)] indicates that even the maximum achievable quenching rate within this range is not sufficiently high to prevent the primary $T \rightarrow O\text{-I}$ ordering during the quenching. Therefore, any cooling regime is, actually, slow within this stoichiometry range. It is slow enough to produce the (110) polytwin structure, consisting of macroscopically large orientational variants of the $O\text{-I}$ phase, which later undergoes secondary $O\text{-I} \rightarrow O\text{-II}$ ordering during the continuing cooling or isothermal annealing in the $O\text{-II}$ field. In this case of macroscopically large domains of the $O\text{-I}$ phase, the effect of the twin boundaries on secondary $O\text{-I} \rightarrow O\text{-II}$ ordering can be ignored and homogeneous ordering can be assumed. This situation has been modeled by considering the secondary $O\text{-I} \rightarrow O\text{-II}$ ordering within a single orientational variant of the $O\text{-I}$ phase. Figures 13(b) and 13(d)–13(f) demonstrate that secondary ordering produces a “glassy” state. The “glassy” state is either stable or metastable, and, thus, like the secondary tweed, can be regarded as a mesophase, the new form of a phase with mesoscale atomic structure. Also like the secondary tweed, it is stabilized by long-range interaction. The “glassy” state consists of nanoscale antiphase domains of the $O\text{-II}$ phase that provide spatial realization of the $(\frac{1}{2}00)$ short-range order. Unlike conventional antiphase domains, the domains forming the “glassy” state do not coarsen.

At $\delta > 0.5$ the deviation from the $O\text{-II}$ phase stoichiometry $\delta = 0.5$ is accommodated by the condensation of extra O atoms on antiphase boundaries [see Figs. 13(e) and 13(f)]. Since all antiphase domains of the

“glassy” state belong to the same orientational variant, the positions of fundamental diffraction spots correspond to the orthorhombic $O\text{-I}$ phase. The only difference is the appearance of wide $(\frac{1}{2}00)$ short-range-order diffuse maxima. According to our results, a “glassy” state can be expected within the $O\text{-II}$ field of the phase diagram, but at stoichiometries $\delta > 0.5$ (at $\delta \leq 0.5$ the secondary tweed is more stable). According to the phase diagram in Fig. 2, the upper bound of the $O\text{-II}$ field at room temperature is $\delta \approx 0.88$. Therefore, the “glassy” state is expected within the range $\sim 0.5 < \delta < \sim 0.88$.

However, the slow cooling of a $O\text{-I}$ phase domain with border stoichiometry $\delta = 0.5$ generates a structure different from those obtained above and below this stoichiometry. The secondary ordering in this material produces the (110) twins of the $O\text{-II}$ phase [Fig. 13(c)]. These twins of the $O\text{-II}$ phase coarsen to sizes commensurate with the size of the computational cell. The antiphase domains of the $O\text{-II}$ phase then reach sizes comparable with a typical thickness of twins [Fig. 13(c)].

Observation seems to confirm these predictions. The highest stoichiometry at which $\{\frac{1}{2}00\}$ diffuse scattering has still been observed is $\delta \sim 0.87$.⁵ This value agrees with the critical stoichiometry for the $O\text{-I} \leftrightarrow O\text{-II}$ transition at room temperature, $\delta = \sim 0.88$, which follows from the phase diagram in Fig. 2.

As follows from our simulation, nanoscale domains of the $O\text{-II}$ phase forming both the “glassy” phase and the secondary tweed cannot coarsen to macroscopic size. Coarsening is possible only at the stoichiometry $\delta = 0.5$ during slow cooling [Fig. 13(c)]. Observations by Reyes-Gasga *et al.*⁵ and by Beyers *et al.*⁶ support this conclusion. These authors were able to obtain macroscopic domains of the $O\text{-II}$ phase only by means of a very special technique that allowed them to maintain the strict stoichiometry $\delta = 0.5$ during the very slow cooling.

It is interesting that another example of the mesophase has been found recently by Kartha *et al.*⁶⁰ These authors have considered the 2D model of the martensitic transformation with infinite elastic moduli anisotropy and local impurity inhomogeneity. The Monte Carlo simulation based on this model has generated the tweed-type mesophase, which is a close analog of the spin-glass state.

C. Heterogeneous ordering within the $O\text{-II}$ field

If the temperature $T_1(c)$ is not too high (i.e., if the stoichiometry is below $\delta \sim 0.5$), the $T \rightarrow O\text{-I}$ ordering may produce a fine polytwin structure during “cooling” through the $O\text{-I}$ field. Our computer simulation shows that the fine polytwin structure [Fig. 5(a)] dramatically affects the secondary-ordering transformation path. It leads to the heterogeneous secondary ordering that starts from the (110) twin boundaries (Figs. 9–12). Because of the strain-induced interaction between the mesoscale structure formed by the (110) twin boundaries and the atomic structure of secondary ordered phases, the twin boundaries promote the formation of metastable superstructure whose dominant superlattice vector is perpendicular to the twin boundary plane, (110). The $2a_0 \times 2a_0$

superstructure generated by the $(\frac{1}{2}\frac{1}{2}0)$ superlattice vector (Fig. 9) and the $2\sqrt{2}a_0 \times 2\sqrt{2}a_0$ (*O*-III) superstructures at $\delta=0.25, 0.375$, and 0.75 generated by the $\{\frac{1}{4}\frac{1}{4}0\}$ superlattice vectors (Figs. 10–12) are examples illustrating this effect. As follows from Fig. 9 ($\delta=0.5$), the $2a_0 \times 2a_0$ phase forms prior to the $2a_0 \times a_0$ phase, although the latter is more stable. Islands of the $2a_0 \times a_0$ (*O*-II) phase appear within the $2a_0 \times 2a_0$ phase on imperfections of the twin boundary. They finally absorb all of the $2a_0 \times 2a_0$ phase. The antiphase boundaries of the $2a_0 \times a_0$ phase limiting the length of -O-Cu-O- chains are readily seen in Figs. 9(b) and 9(c). If twin boundaries are perfect, the $2a_0 \times 2a_0 \rightarrow 2a_0 \times a_0$ rearrangement does not occur and the stable $2a_0 \times a_0$ phase does not appear (of course, it may appear due to the fluctuation and nucleation mechanism, which is not described by the kinetic equations of our model). The observation of the $2a_0 \times 2a_0$ phase is probably difficult since it is a transient phase preceding the *O*-II phase formation under the special condition of the existence of developed (110) twin boundaries at the moment of secondary ordering [Fig. 9(a)]. Nevertheless, there are reports of observation of this phase.⁵

The *O*-III phase is stable. Indeed, if the stoichiometry deviates from $\text{YBa}_2\text{Cu}_3\text{O}_{6.5}$, it cannot be accommodated within the *O*-II phase unit cell and an alternative transformation route, the decomposition, is suppressed by the long-range repulsion. Then, the tertiary ordering accommodating the current stoichiometry should develop. To find the ordering temperature and the structure of the tertiary ordered *O*-III phase, we have to investigate the function

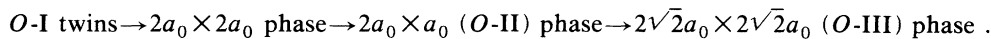
$$V(\mathbf{k}) = \frac{V_{22}(\mathbf{k}) + V_{22}(\mathbf{k} - \mathbf{k}_1)}{2},$$

where $\mathbf{k}_1 = (2\pi/a_0)(\frac{1}{2}00)$. The minimum of $V(\mathbf{k})$ determines the superlattice vector of the tertiary ordered phase (see, for example, Ref. 18). The function $V(\mathbf{k})$ evaluated for the interaction potentials chosen in this study has its minimum at $\mathbf{k}_3 = (2\pi/a_0)\{\frac{1}{4}\frac{1}{4}0\}$. The value of $T_3(c)$ can be found from the value of the $\min[V(\mathbf{k})] = V(\mathbf{k}_3)$ using the equation

$$T_3(c) = -\frac{4c(1-4c)V(\mathbf{k}_3)}{k_B},$$

which is similar to Eq. (24). The dependence $T_3(c)$ is shown in the phase diagram in Fig. 2 by the dashed line. The tertiary ordered *O*-III phase generated by the concentration waves $(2\pi/a_0)\{\frac{1}{4}\frac{1}{4}0\}$ is characterized by the $\{\frac{1}{4}\frac{1}{4}0\}$ superlattice diffraction spots in addition to $\{\frac{1}{2}00\}$ superlattice spots of the secondary ordered *O*-II phase. The unit cell corresponding to such a diffraction pattern is $2\sqrt{2}a_0 \times 2\sqrt{2}a_0$.

Our computer-simulation results for $\delta = \frac{1}{4}, \frac{3}{8}$, and $\frac{3}{4}$ are in a complete agreement with the above concentration-wave thermodynamic analysis. If $T > T_3(c)$, the sequence of the secondary-ordering transformations, *O*-I twins $\rightarrow 2a_0 \times 2a_0$ phase $\rightarrow 2a_0 \times a_0$ phase, is the same as in the case of $\delta=0.5$ shown in Fig. 9. But, if $T < T_3(c)$, the *O*-II \rightarrow *O*-III tertiary ordering takes place. It is realized as the last step of the transformation sequence



Figures 10–12 show the positions of O atoms in the $2\sqrt{2}a_0 \times 2\sqrt{2}a_0$ unit cell of the tertiary ordered *O*-III phase and the $\{\frac{1}{4}\frac{1}{4}0\}$ and $\{\frac{1}{2}00\}$ superlattice maxima on its diffraction pattern. The deviation from the exact stoichiometries, $\delta = \frac{1}{4}$ and $\delta = \frac{3}{4}$, is accommodated by changing the number of O atoms within the $2\sqrt{2}a_0 \times 2\sqrt{2}a_0$ unit cell (Fig. 12 for $\delta=0.375$).

Microstructures presented in Figs. 10–12 clearly indicate that the *O*-III structure is formed on the basis of the parent *O*-II phase. Both phases, *O*-II and *O*-III, as expected, inherit the orientation of -O-Cu-O- chains in twins of initial *O*-I polytwin structure. Unit cells of the *O*-III phase, however, contain only fragments of these chains, the lengths of which are dictated by the current stoichiometry [Figs. 10(b), 11(b), and 12(b)].

Although the $2\sqrt{2}a_0 \times 2\sqrt{2}a_0$ structure simulated at $\delta = \frac{3}{4}$ is presented in Fig. 10, we do not expect that it could be formed in reality. Fast cooling and even quenching are not fast enough to ensure its appearance at this stoichiometry—this stoichiometry is outside the relevant range below $\delta \sim 0.5$ at which the heterogeneous ordering discussed here occurs. The stoichiometry $\delta = \frac{3}{4}$ is within the range where the “glassy” phase is expected.

Alario-Franco *et al.*,^{8,7} Reyes-Gasga *et al.*,⁵ and

Sonntag *et al.*⁹ have reported the observation of $\{\frac{1}{4}\frac{1}{4}0\}$ extra spots in the diffraction pattern of nonstoichiometric $\text{YBa}_2\text{Cu}_3\text{O}_{6+\delta}$. These spots were interpreted as the superlattice reflections generated by the ordered phase with the $2\sqrt{2}a_0 \times 2\sqrt{2}a_0$ unit cell. The intensity measurements for the $2\sqrt{2}a_0 \times 2\sqrt{2}a_0$ structure in $\text{YBa}_2\text{Cu}_3\text{O}_{6.35}$ were made in the single-crystal neutron-diffraction study.⁹ We note that the atomic structure of the $2\sqrt{2}a_0 \times 2\sqrt{2}a_0$ phase predicted in our computer simulation for $\delta=0.375$ differs from the structure proposed in Ref. 9 for the close stoichiometry, $\delta=0.35$. But, being different, both structures are equally well fitted to the observed diffraction pattern. Unfortunately, the intensity single-phase measurements made in Ref. 9 do not lend us an argument sufficient to make a choice, since the investigated samples actually have not been in a single-phase state consisting of a single orientational domain (to get a single-domain state, the samples should be untwinned). The presence of two twin-related orientational variants of the $2\sqrt{2}a_0 \times 2\sqrt{2}a_0$ phase would result in a superposition of their Patterson synthesis, which obscures the structure identification.

It should be mentioned that Krekels *et al.*⁶¹ and Werdner *et al.*⁶² proposed two different hypotheses based on the

thin-film electron-microdiffraction pictures, which, unlike later work by Sonntag *et al.*,⁹ do not relate the $2\sqrt{2}a_0 \times 2\sqrt{2}a_0$ phase to oxygen ordering. Krekels *et al.*⁶¹ assumed that the $\{\frac{1}{4}\frac{1}{4}0\}$ superlattice spots are caused by the Jahn-Teller effect upon heating (this hypothesis requires additional clarification, since, according to conventional theory, the Jahn-Teller transition should occur upon cooling and, being displacive, should develop instantaneously with the sound velocity speed).

On the other hand, Werder *et al.*⁶² assumed that the $2\sqrt{2}a_0 \times 2\sqrt{2}a_0$ phase is caused by ordering of Cu (and, probably, Ba) vacancies. However, this fact alone is not sufficient to rule out that oxygen ordering may be also involved and may even drive the entire ordering process.

These two different mechanisms, proposed in Refs. 61 and 62 on the basis of thin-film electron microdiffraction, are also different from the oxygen-ordering mechanism proposed by Sonntag *et al.*⁹ on the basis of the quantitative interpretation of the neutron-diffraction-intensity data obtained from the single-crystal bulk sample. Although our computer simulation cannot resolve this contradiction, it nevertheless tips the argument in favor of the oxygen-ordering mechanism of $2\sqrt{2}a_0 \times 2\sqrt{2}a_0$ phase formation.^{5,7-9}

The O-O interaction potentials used in this computer simulation are just the first reasonable approximation that can be improved when more experimental data and the first-principles calculational results become available. An example of such a calculation for the configurational ground-state energy of the ordered structures in $\text{YBa}_2\text{Cu}_3\text{O}_{6+\delta}$ was made by Stern and Wille.^{37,63} However, the successful simulation of unusual transformations in $\text{YBa}_2\text{Cu}_3\text{O}_{6+\delta}$ seems to show that the assumed potentials embody the main features of the O-O interaction: its predominantly long-range repulsive character, associated with the electrostatic interaction, and its long-range dipole-dipolelike behavior, associated with the strain-induced interaction.

However, certain limitations of the assumed interaction model should be mentioned. Besides the "glassy" or-

thorhombic phase, which accommodates the current stoichiometry, another accommodation mechanism, the formation of a Magneli-phase series, $\text{YBa}_2\text{Cu}_3\text{O}_{7-n/(2n+1)}$,⁶⁴ is also possible. A question, which of these phases, "glassy" phase or Magneli phase, is more stable at different temperatures, could be resolved by the comparison of their free energies. We made such a comparison for the structure shown in Fig. 13(e) and for the $5a_0 \times a_0$ Magneli phase with the same $\text{YBa}_2\text{Cu}_3\text{O}_{6.6}$ stoichiometry. At room temperature the free energies of these phases practically coincide, although the free energy of the "glassy" state proves to be $\sim 0.4\%$ less than that of the Magneli phase. A relative stability of these states proves to be very sensitive to the details of the interaction potential. A small "tuning" of the parameters determining the O-O interaction potentials, Eq. (20), can, of course, reverse the situation and make the Magneli phase more stable. This shows that the further progress would require the refinement of the interaction model. What is clear, however, is the following. Even if the $5a_0 \times a_0$ Magneli phase is more stable at low temperatures than the "glassy" phase, the "glassy" phase would, nevertheless, appear first upon the cooling. Indeed, the "glassy" state forms immediately below $T_2(c)$, where the temperature is too high for the Magneli phase to be stable. Therefore, the Magneli phase may be formed only later, by a comparatively slow nucleation and growth mechanism.

ACKNOWLEDGMENTS

We gratefully acknowledge the support by Division of Materials Science, U.S. Department of Energy, under Grant No. DE-FG05-90ER45430. We are grateful to Dr. Long-Qing Chen and Mr. Yunzhi Wang for numerous discussions and help. The simulation was performed on CONVEX, SRAC, College of Engineering, Rutgers University, and on the Cray-YMP at the Pittsburgh Supercomputing Center.

¹G. Van Tendeloo, H. W. Zandbergen, and S. Amelinckx, *Solid State Commun.* **63**, 389 (1987); **63**, 603 (1987).

²C. H. Chen, J. Werder, L. F. Scheemeyer, P. Gallagher, and J. W. Waszczak, *Phys. Rev. B* **38**, 2888 (1988).

³D. J. Werder, C. H. Chen, R. J. Cava, and B. Batlogg, *Phys. Rev. B* **37**, 2317 (1988).

⁴R. M. Fleming, L. F. Schneenyer, P. K. Gallagher, B. Batlogg, L. W. Rupp, and J. W. Waszczak, *Phys. Rev. B* **37**, 7920 (1988).

⁵J. Reyes-Gasga, T. Krekels, G. Van Tendeloo, J. Van Landuyt, S. Amelinckx, W. H. M. Bruggink, and H. Werweij, *Physica C* **159**, 831 (1989).

⁶R. Beyers, B. T. Ahn, G. Gorman, V. Y. Lee, S. S. P. Parkin, M. L. Ramirez, K. P. Roche, X. Vazques, T. M. Gur, and R. A. Haggins, *Nature (London)* **340**, 619 (1989).

⁷C. Chaillout, M. A. Alario-Franco, J. J. Capponi, J. Chenavas, J. L. Hodeau, and M. Marezio, *Phys. Rev. B* **36**, 7118 (1987).

⁸M. A. Alario-Franco, C. Chaillout, J. J. Capponi, and J. Chenavas, *Mater. Res. Bull.* **22**, 1685 (1987).

⁹R. Sonntag, D. Hohlwein, T. Brucke, and G. Collin, *Phys. Rev. Lett.* **66**, 1497 (1991).

¹⁰Y. Zhu, A. R. Moodenbaugh, M. Suenaga, and J. Taftø, *Physica C* **167**, 363 (1990).

¹¹A. M. Stoneham and J. H. Harding, *Annu. Rev. Phys. Chem.* **37**, 53 (1986); in *Computer Simulation of Solids*, edited by C. R. A. Catlow and W. C. Mackrodt, Lecture Notes in Physics Vol. 166 (Springer-Verlag, New York, 1982).

¹²S. Valkealahty and D. O. Welch, *Physica C* **162-164**, 540 (1989).

¹³R. C. Baetzold, *Phys. Rev. B* **38**, 11 304 (1988).

¹⁴R. C. Baetzold, *Phys. Rev. B* **42**, 56 (1990).

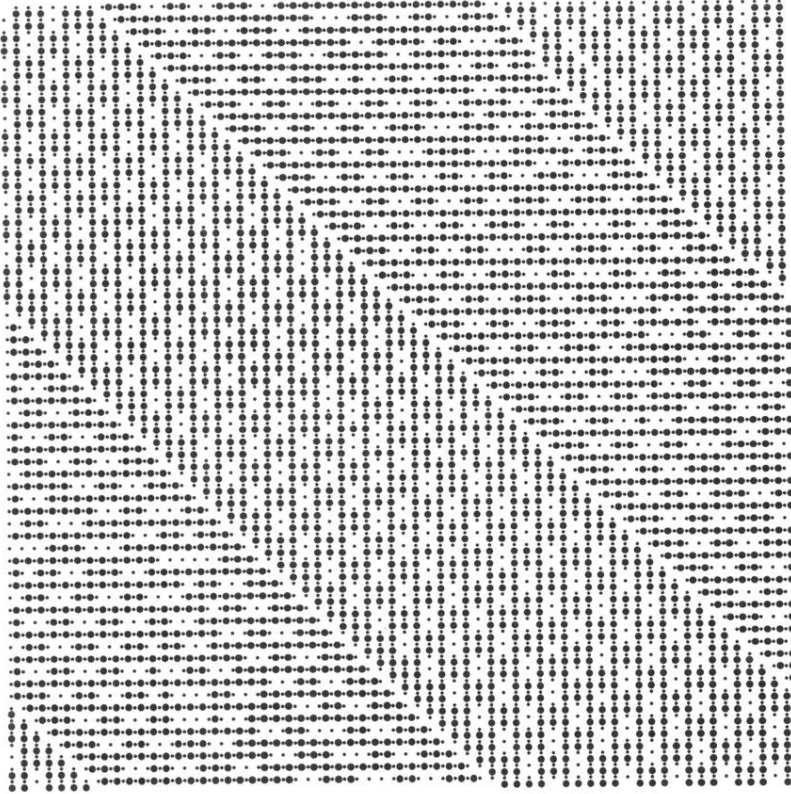
¹⁵A. A. Aligia, A. G. Rojo, and B. R. Alascio, *Phys. Rev. B* **38**, 6604 (1988).

¹⁶A. A. Aligia, J. Garces, and H. Bonadeo, *Phys. Rev. B* **42**, 10 226 (1990).

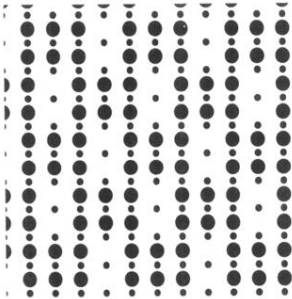
¹⁷A. G. Khachatryan and G. A. Shatalov, *Zh. Eksp. Teor. Fiz.* **56**, 1037 (1969) [*Sov. Phys. JETP* **29**, 557 (1969)].

¹⁸A. G. Khachatryan, *The Theory of Structural Transforma-*

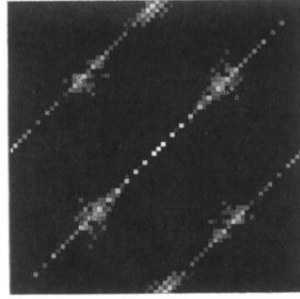
- tion in Solids* (Wiley, New York, 1983).
- ¹⁹A. L. Roitburd, *Fiz. Tverd. Tela* (Leningrad) **10**, 3619 (1968) [*Sov. Phys. Solid State* **10**, 2870 (1969)].
- ²⁰R. Beyers, G. Lim, E. M. Engler, R. J. Savoy, T. M. Shaw, T. R. Dinger, W. J. Gallagher, and R. L. Sandstrom, *Appl. Phys. Lett.* **50**, 1918 (1987).
- ²¹M. Sarikaya, R. Kikuchi, and I. A. Aksay, *Physica C* **152**, 161 (1988).
- ²²S. Amelinckx, G. Van Tendeloo, and J. Van Landuyt (unpublished).
- ²³Y. Xu, M. Suenaga, J. Tafto, R. L. Sabatini, A. R. Moodenbaugh, and P. Zolliker, *Phys. Rev. B* **39**, 6667 (1989).
- ²⁴G. Van Tendeloo, D. Broddin, H. W. Zandbergen, and S. Amelinckx, *Physica C* **167**, 627 (1990).
- ²⁵Yimey Zhu, M. Suenaga, and A. R. Moodenbaugh, *Philos. Mag.* **62**, 51 (1990).
- ²⁶Y. Zhu, M. Suenaga, and A. R. Moodenbaugh, *Ultramicroscopy* **37**, 341 (1991).
- ²⁷Yimey Zhu, M. Suenaga, J. Tafto, and D. O. Welch, *Phys. Rev. B* **44**, 2871 (1991).
- ²⁸L. T. Wille and D. de Fontaine, *Phys. Rev. B* **37**, 2227 (1988).
- ²⁹L. T. Wille, A. Berera, and D. de Fontaine, *Phys. Rev. Lett.* **60**, 1065 (1988).
- ³⁰J. M. Sanchez, F. Mejia-Lira, and J. L. Moran-Lopez, *Phys. Rev. B* **37**, 3678 (1988).
- ³¹R. Kikuchi and J. S. Choi, *Physica C* **160**, 347 (1989).
- ³²Z. X. Cai and S. D. Mahanti, *Phys. Rev. B* **40**, 6558 (1988).
- ³³L. T. Wille, *Phys. Rev. B* **40**, 6941 (1989).
- ³⁴C. P. Burmeister and L. T. Wille, *Phys. Rev. B* **40**, 8795 (1989).
- ³⁵C. C. A. Gunther, P. A. Rikvold, and M. A. Novotny, *Phys. Rev. B* **42**, 10738 (1990).
- ³⁶H. F. Poulsen, N. H. Andersen, J. V. Andersen, H. Bohr, and O. G. Mouritsen, *Phys. Rev. Lett.* **66**, 465 (1991).
- ³⁷P. Sterne and L. T. Wille, *Physica C* **162-164**, 223 (1989).
- ³⁸A. G. Khachaturyan, *Fiz. Tverd. Tela* (Leningrad) **9**, 2595 (1967) [*Sov. Phys. Solid State* **9**, 2040 (1968)].
- ³⁹S. Semenovskaya and A. G. Khachaturyan, *Phys. Rev. Lett.* **67**, 2223 (1991).
- ⁴⁰L. Q. Chen and A. G. Khachaturyan, *Phys. Rev. B* **44**, 4681 (1991).
- ⁴¹Y. Z. Wang, L. Q. Chen, and A. G. Khachaturyan, *Scr. Metall. Mater.* **25**, 1969 (1991).
- ⁴²Y. Z. Wang, L. Q. Chen, and A. G. Khachaturyan, *Scr. Metall. Mater.* **25**, 1387 (1991).
- ⁴³V. G. Vaks, A. I. Larkin, and S. A. Pikin, *Zh. Eksp. Teor. Fiz.* **51**, 361 (1966) [*Sov. Phys. JETP* **51**, 240 (1966)].
- ⁴⁴R. A. Suris, *Fiz. Tverd. Tela* (Leningrad) **4**, 1154 (1962) [*Sov. Phys. Solid State* **4**, 850 (1962)].
- ⁴⁵A. G. Khachaturyan, *Fiz. Tverd. Tela* (Leningrad) **5**, 750 (1963) [*Sov. Phys. Solid State* **5**, 548 (1963)].
- ⁴⁶A. G. Khachaturyan and G. A. Shatalov, *Acta Metall.* **23**, 1089 (1975).
- ⁴⁷S. J. Rothman, J. L. Routbort, and U. Welp, *Phys. Rev. B* **44**, 2326 (1991).
- ⁴⁸R. J. Cava, B. Batlogg, C. H. Chen, E. A. Reitman, S. M. Zahurak, and D. Werder, *Nature* (London) **329**, 423 (1987).
- ⁴⁹J. D. Jorgensen, M. A. Beno, D. G. Hinks, L. Soderholm, H. J. Volin, R. L. Hitterman, J. D. Grace, I. K. Schuller, C. V. Serge, K. Zhang, and M. S. Kleefish, *Phys. Rev. B* **36**, 3608 (1987).
- ⁵⁰M. Blanter and A. G. Khachaturyan, *Phys. Status Solidi A* **60**, 64 (1980).
- ⁵¹K. Huang, *Proc. R. Soc. London, Ser. A* **190**, 102 (1947).
- ⁵²A. G. Khachaturyan, *Fiz. Tverd. Tela* (Leningrad) **4**, 2840 (1962) [*Sov. Phys. Solid State* **4**, 2081 (1962)].
- ⁵³L. E. Tanner, *Philos. Mag.* **14**, 111 (1966).
- ⁵⁴D. E. Laughlin, R. Sinclair, and L. Tanner, *Scr. Metall.* **14**, 373 (1980).
- ⁵⁵I. M. Robertson and C. M. Wayman, *Philos. Mag. A* **48**, 421 (1983); **48**, 443 (1983); **48**, 629 (1983).
- ⁵⁶S. J. Rothman, J. L. Routbort, and J. E. Baker, *Phys. Rev. B* **40**, 8852 (1989).
- ⁵⁷B. W. Veal, A. P. Paulikas, Hoydoo Yoo, Hao Shi, Y. Fang, and J. W. Downey, *Phys. Rev. B* **42**, 4770 (1990).
- ⁵⁸G. Van Tendeloo and S. Amelinckx (unpublished).
- ⁵⁹M. Sugiyama, R. Ohshima, and F. E. Fujita, *Trans. Jpn. Inst. Met.* **27**, 719 (1986).
- ⁶⁰S. Kartha, T. Castán, J. A. Krumhansl, and J. P. Sethna, *Phys. Rev. Lett.* **67**, 3630 (1991).
- ⁶¹T. Krekels, T. S. Shi, J. Reyes-Gasga, G. Van Tendeloo, J. Van Landuyt, and S. Amelinckx, *Physica C* **167**, 677 (1990).
- ⁶²D. J. Werder, C. H. Chen, and G. P. Espinosa, *Physica C* **173**, 285 (1991).
- ⁶³P. A. Sterne and L. T. Wille (unpublished).
- ⁶⁴A. G. Khachaturyan and J. W. Morris, Jr., *Phys. Rev. Lett.* **61**, 215 (1988).



(a)

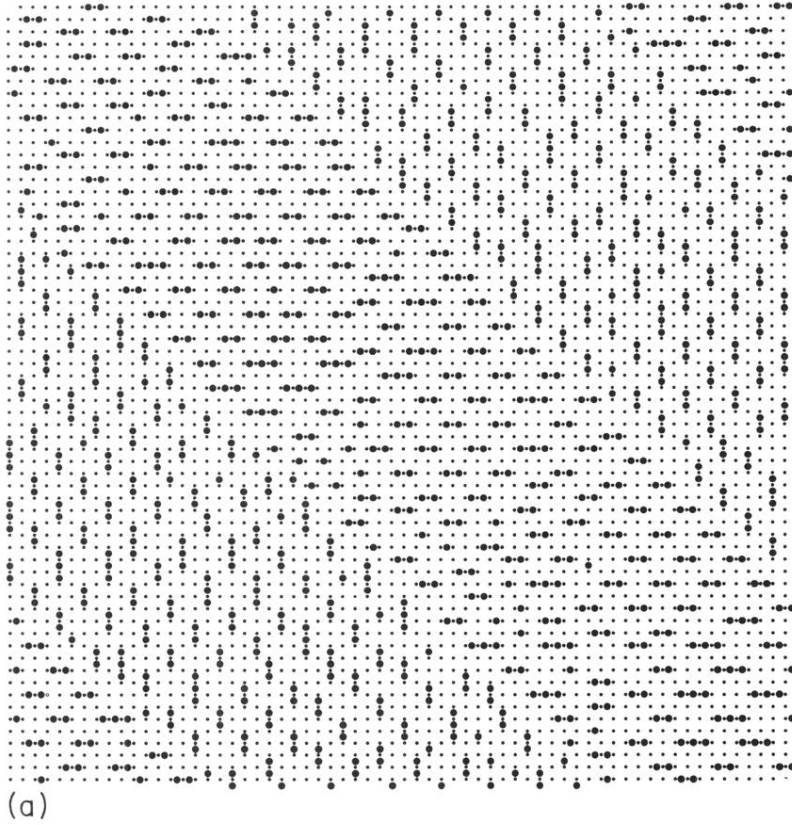


(b)

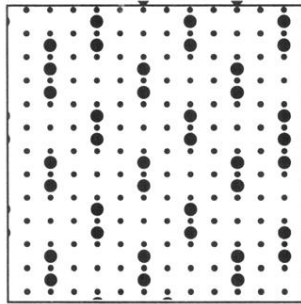


(c)

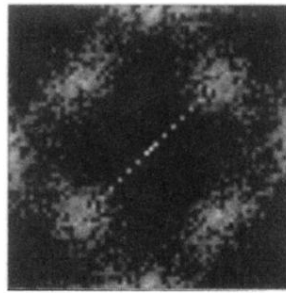
FIG. 10. Simulated *O*-III structure in $\text{YBa}_2\text{Cu}_3\text{O}_{6.75}$. Initial *O*-I polytwinned structure is formed during the high-temperature annealing at $T/T_1=0.78$, $t^*=64$. The following annealings resulting in the secondary and tertiary ordering were at the temperatures $T/T_2=0.61$ ($t^*=128$) and $T/T_2=0.5$ ($t^*=128$). (a) The final tertiary ordered microstructure of the *O*-III ($2\sqrt{2}a_0 \times 2\sqrt{2}a_0$) phase. (b) An enlarged fragment of the structure shown in (a). (c) Intensity distribution within the first Brillouin zone of the $a_0 \times a_0$ host lattice on a logarithmic scale. Four maxima nearest the zone origin are of $\{\frac{1}{4} \frac{1}{4}\}$ type, two maxima on the zone boundaries are of $\{\frac{1}{2} 00\}$ type, and streaks along the $\langle 110 \rangle$ directions are generated by twin boundaries. The model crystal consists of 64×64 unit cells.



(a)



(b)



(c)

FIG. 11. Simulated *O*-III structure in $\text{YBa}_2\text{Cu}_3\text{O}_{6.25}$. Initial *O*-I polytwinned structure is formed during the high-temperature annealing at $T/T_1=0.83$, $t^*=64$. The following annealings resulting in the secondary and tertiary ordering were at the temperatures $T/T_2=0.72$ ($t^*=128$) and $T/T_2=0.58$ ($t^*=128$). (a) The final tertiary ordered microstructure of the *O*-III ($2\sqrt{2}a_0 \times 2\sqrt{2}a_0$) phase. (b) An enlarged fragment of the structure shown in (a). (c) Intensity distribution within the first Brillouin zone of the $a_0 \times a_0$ host lattice on a logarithmic scale. Four maxima nearest the zone origin are of $\{\frac{1}{4}\frac{1}{4}0\}$ type, four maxima on the zone boundaries are of $\{\frac{1}{2}00\}$ type, and streaks along the $\langle 110 \rangle$ directions are generated by twin boundaries. The model crystal consists of 64×64 unit cells.

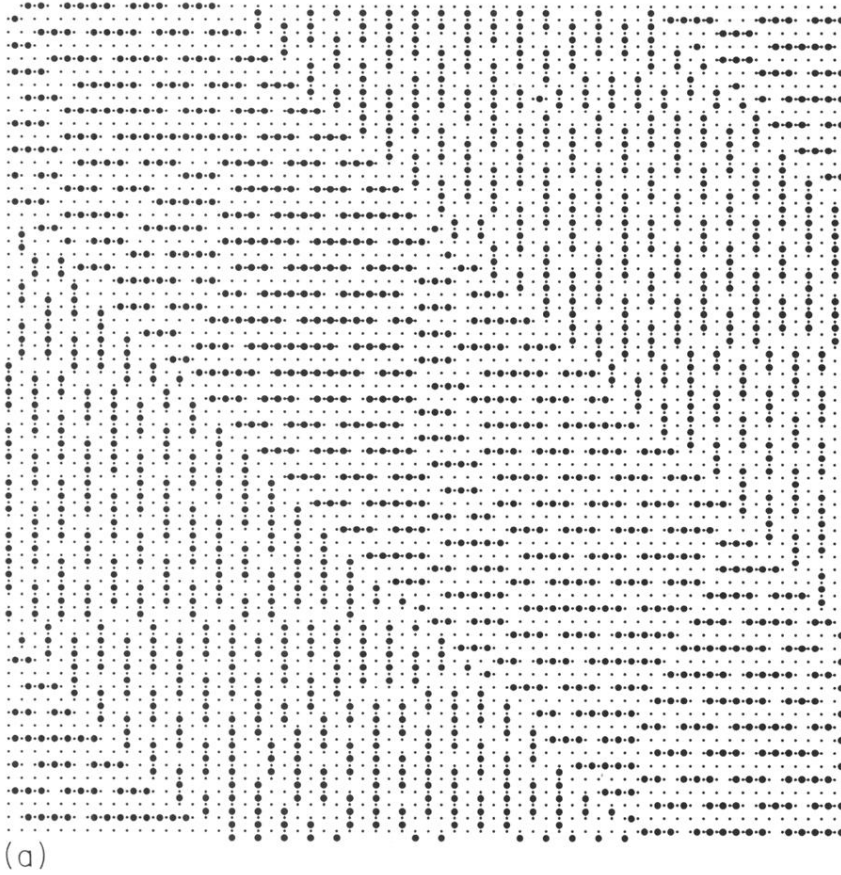
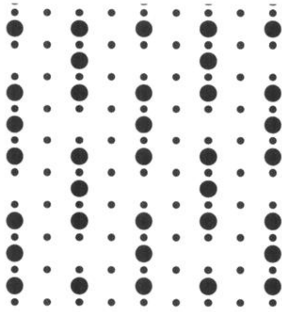
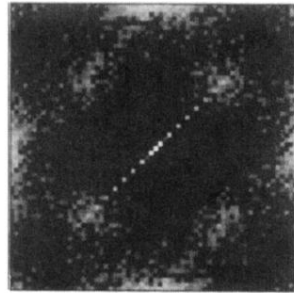


FIG. 12. Simulated *O*-III structure in $\text{YBa}_2\text{Cu}_3\text{O}_{6.375}$ ($\delta = \frac{3}{8}$). Initial *O*-I polytwinned structure was formed during the high-temperature annealing at $T/T_1 = 0.84$, $t^* = 64$. The next annealings resulting in the secondary and tertiary ordering were at the temperatures $T/T_2 = 0.75$ ($t^* = 32$), $T/T_2 = 0.42$ ($t^* = 128$), and $T/T_2 = 0.32$ ($t^* = 128$). (a) The final tertiary ordered microstructure of the *O*-III ($2\sqrt{2}a_0 \times 2\sqrt{2}a_0$) phase. (b) An enlarged fragment of the structure shown in (a). (c) Intensity distribution within the first Brillouin zone of the $a_0 \times a_0$ host lattice on a logarithmic scale. Four maxima nearest the zone origin are of $\{\frac{1}{4} \frac{1}{4} 0\}$ type, four maxima on the zone boundaries are of $\{\frac{1}{2} 0 0\}$ type, and streaks along the $\langle 110 \rangle$ directions are generated by twin boundaries. The model crystal consists of 64×64 unit cells.

(a)



(b)



(c)

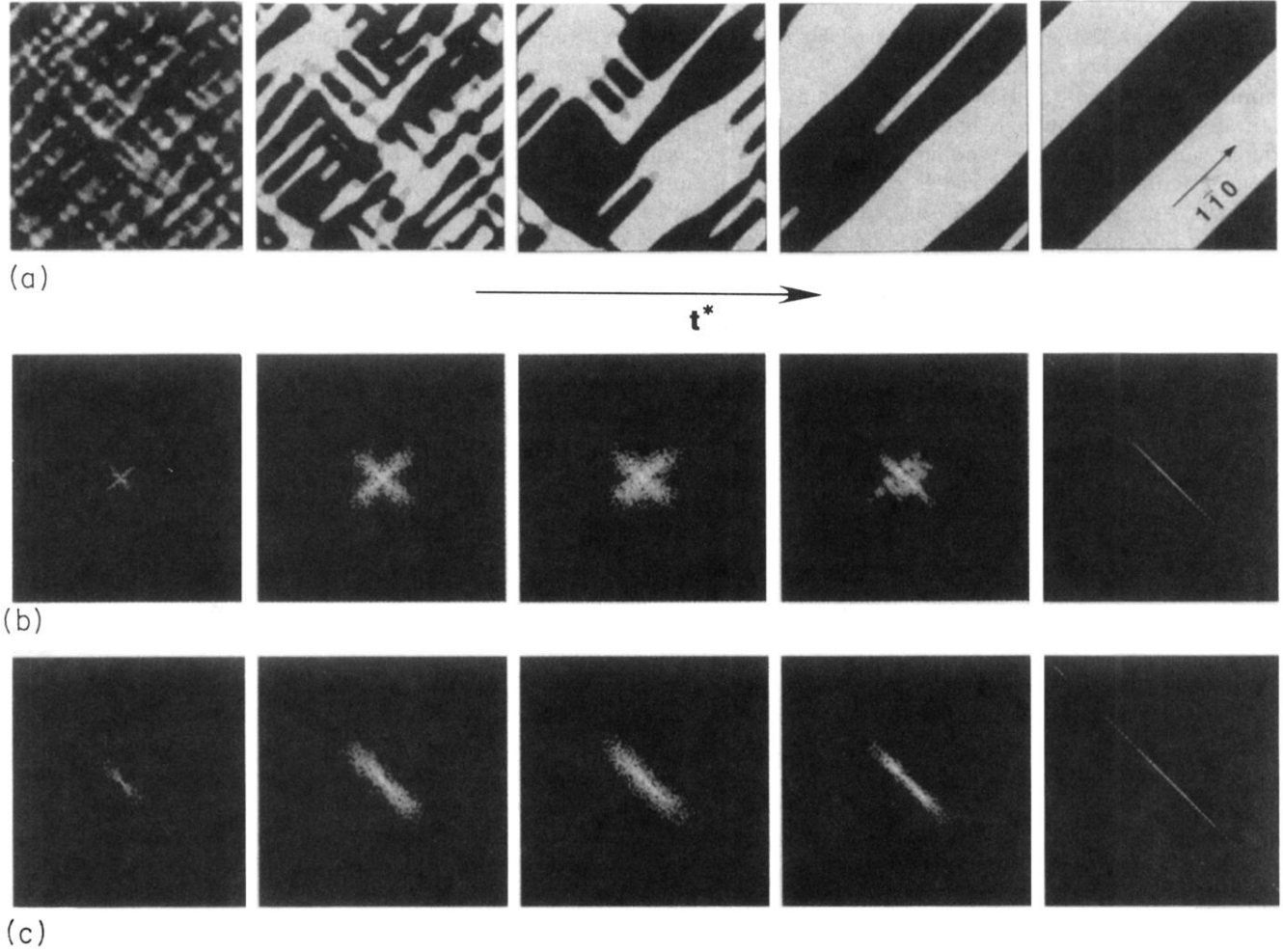
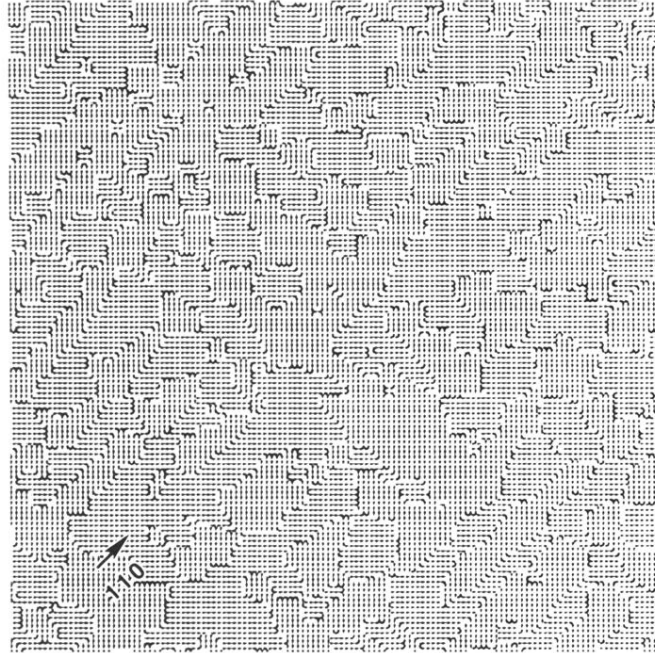
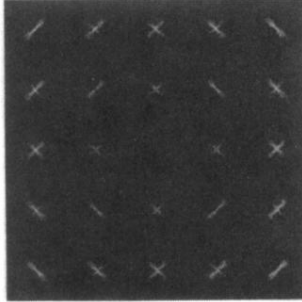


FIG. 3. (a) Simulated temporal isothermal evolution of microstructure in $\text{YBa}_2\text{Cu}_3\text{O}_7$ at the temperature $T/T_1=0.79$. The transformation reduced time t^* is equal to 4, 12, 40, 80, and 120 (from left to right). Two types of orientation domains are characterized by a value of the LRO parameter, $\eta=[n(1,\mathbf{r})-n(2,\mathbf{r})]/2c$ [Eq. (38)]. Regions with positive η describe orientation domains of the first type with preferred occupation of sites of the first interstitial sublattice (light-to-white color). Regions with negative η characterize domains of the second type (black). (b)–(c) are the corresponding strain-induced scattering at $t^*=2.5, 4, 12, 80,$ and 120 (from left to right) around (a) (400) and (b) (440) fundamental diffraction spots. The intensity $I_{\text{stat}}(\mathbf{k})$ [Eq. (37)] is shown on a logarithmic scale. The system size is 128×128 unit cells.



(a)

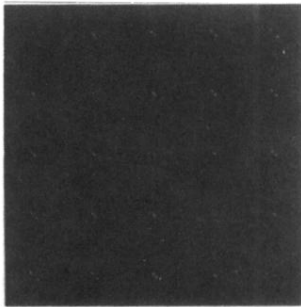


(b)

FIG. 4. (a) Atomic representation of the tweed structure in $\text{YBa}_2\text{Cu}_3\text{O}_7$ shown in Fig. 3(a) for $t^*=4$. The small black circles are Cu atoms, and the larger dark circles are O atoms, which are shown if the occupation probability $n(p, \mathbf{r}) > c$ ($c=0.5$ for $\text{YBa}_2\text{Cu}_3\text{O}_7$). (b) The corresponding strain-induced diffuse scattering in the (001) reciprocal-lattice plane from the tweed structure ($t^*=4$). The (000) origin is in the center of the diffraction pattern. Diffuse maxima are around the Bragg peaks. The intensity $I_{\text{stat}}(\mathbf{k})$ [Eq. (37)] is shown on a logarithmic scale. The diffuse maxima are enlarged by the factor 1.6. The model crystal consists of 128×128 unit cells.

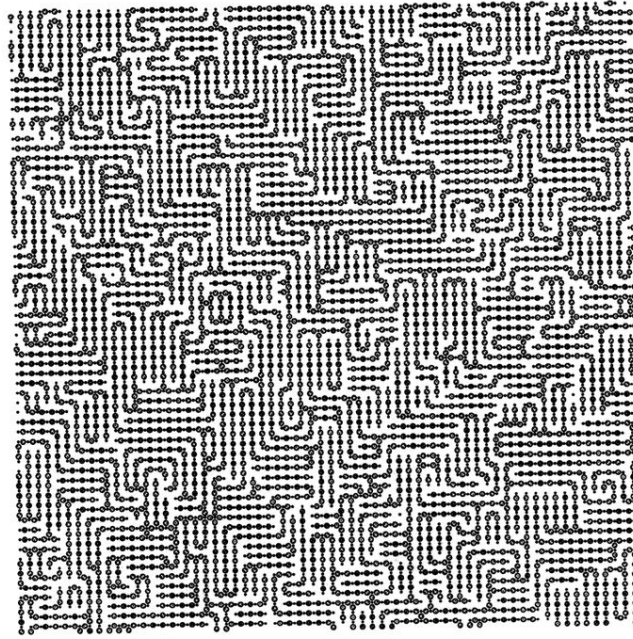


(a)

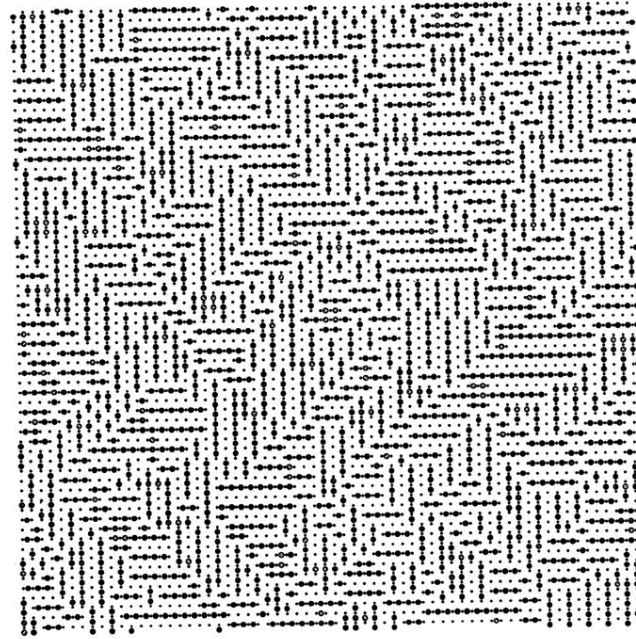


(b)

FIG. 5. (a) Atomic representation of the twin structure in $\text{YBa}_2\text{Cu}_3\text{O}_7$ shown in Fig. 3(a) for $t^* = 120$. The O atoms are shown if $n(p, \mathbf{r}) > c$ ($c = 0.5$). (b) The corresponding diffraction pattern described by the intensity $I(\mathbf{k})_{\text{stat}}$ [Eq. (37)] in the (001) reciprocal-lattice plane. It demonstrates the twin-related splitting of the Bragg peaks. The origin (000) is in the center of the pattern. The diffuse maxima are enlarged by the factor 2.1. Intensities less than 5% of $I(\mathbf{k}=\mathbf{0})_{\text{stat}}$ are not shown. The model crystal consists of 128×128 unit cells.



(a)



(b)

FIG. 7. The tweed pattern formation in $\text{YBa}_2\text{Cu}_3\text{O}_{6.5}$ produced by isothermal “annealing” the T phase at $T/T_2=0.72$. (a) the primary tweed consisting of O -I domains (the annealing time $t^*=1.2$), and (b) the secondary tweed consisting of O -II domains formed from the primary tweed domains (the annealing time $t^*=64$). Small black circles are Cu atoms, and larger dark circles are O atoms that are shown if the occupation probability $n(p, \mathbf{r}) > c$ ($c=0.25$ for $\text{YBa}_2\text{Cu}_3\text{O}_{6.5}$). The model crystal consists of 64×64 unit cells.

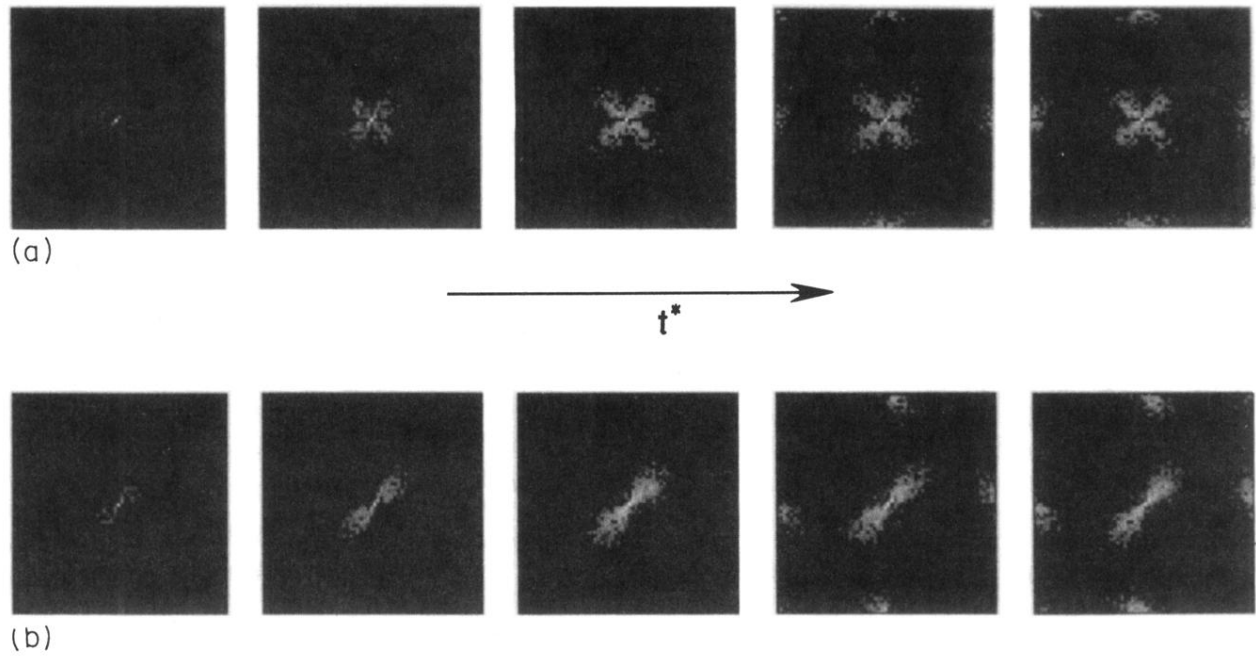


FIG. 8. Evolution of the strain-induced diffuse scattering from $\text{YBa}_2\text{Cu}_3\text{O}_{6.5}$ at the temperature $T/T_2=0.72$. The intensity distribution $I_{\text{stat}}(\mathbf{k})$ (on a logarithmic scale) is shown within the first Brillouin zones with centers in (a) (400) and (b) (440) Bragg maxima. The diffuse maxima are situated in the center of the Brillouin zones. Different states along the transformation path correspond to the reduced times t^* : 0.8, 1.2, 3, 8, and 64 (from left to right). The primary tweed structure is formed at $t^* < 2.5$; the secondary tweed structure appears at $t^* \geq 2.5$. $O\text{-I} \rightarrow O\text{-II}$ ordering is revealed by appearing the additional $\{\frac{1}{2}00\}$ -type diffuse maxima on the zone boundaries (for $t^* = 8$ and 64). The model crystal consists of 64×64 unit cells.